Rafael André Valente Lemos

Carbon nanotubes-reinforced cell-derived matrix-silk fibroin hierarchical scaffolds for bone tissue engineering applications

Carbon nanotubes-reinforced cell-derived-silk fibroin hierarchical scaffolds for bone tissue engineering

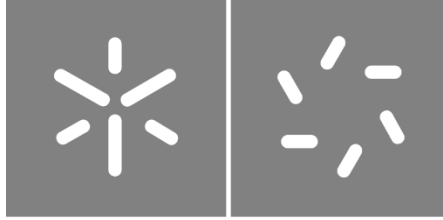Rafael André Valente Lemos

UMinho | 2021

julho de 2021

Universidade do Minho
Escola de Ciências

Rafael André Valente Lemos

Carbon nanotubes-reinforced cell-derived matrix-silk fibroin hierarchical scaffolds for bone tissue engineering applications

Dissertação de Mestrado

Mestrado em Biofísica e Bionanossistemas

Trabalho efetuado sob a orientação de:

Doutor Joaquim Miguel Oliveira

Professor Doutor Paulo José Gomes Coutinho

julho de 2021

DIREITOS DE AUTOR E CONDIÇÕES DE UTILIZAÇÃO DO TRABALHO POR TERCEIROS

Este é um trabalho académico que pode ser utilizado por terceiros desde que respeitadas as regras e boas práticas internacionalmente aceites, no que concerne aos direitos de autor e direitos conexos. Assim, o presente trabalho pode ser utilizado nos termos previstos na licença abaixo indicada.

Caso o utilizador necessite de permissão para poder fazer um uso do trabalho em condições não previstas no licenciamento indicado, deverá contactar o autor, através do RepositóriUM da Universidade do Minho.

Licença concedida aos utilizadores deste trabalho

Agradecimentos

Gostaria de agradecer ao Professor Rui L. Reis pela oportunidade de desenvolver a minha dissertação de mestrado no Instituto de Investigação em Biomateriais, Biodegradáveis e Biomiméticos (I3B's), na Universidade do Minho.

Ao meu orientador, Doutor J. Miguel Oliveira, por me conceder esta oportunidade, por toda a ajuda e por toda a confiança que depositou em mim ao longo deste projeto.

À Doutora Raquel Maia, uma das melhores pessoas que já tive o prazer de conhecer, a quem estarei eternamente grato por toda a motivação, ajuda, palavras de apoio, pela enorme paciência, por todos os ensinamentos que me transmitiu sem os quais a realização do trabalho não seria possível e sobretudo por ser um exemplo para mim tanto como pessoa como na ciência. Se um dia tiver o privilégio de ensinar alguém, e se sobre os meus alunos tiver metade da influência que a Raquel teve sobre mim, já me sentiria realizado.

Ao Professor Paulo Coutinho por aceitar orientar este projeto.

À ação Research and Inovation Staff Exchanges (RISE) (ação H2020 Marie Skłodowska-Curie) pelos fundos obtidos através do projeto BAMOS (H2020-MSCA-RISE-2016-734156) que ajudaram a realizar este projeto.

Ao Doutor João Costa, Doutora Viviana Ribeiro, e Lara Pierantoni por toda a ajuda e conselhos que deram ao longo deste projeto.

Aos meus pais e ao meu irmão, por sempre me apoiarem ao longo do meu percurso académico, por todos sacrifícios e todo o amor.

Aos meus amigos, a minha segunda família, por todos os momentos de boa disposição que me ajudaram nos momentos menos bons.

Ao pessoal da Biblioteca, poço de sabedoria e humor, por todos os bons momentos passados, das discussões científicas e filosóficas até aos momentos mais parvos, cada um deles levarei comigo.

À minha namorada Ana, meu orgulho, porto de abrigo e minha motivação, que me ajudou a ultrapassar os piores momentos e fez questão de celebrar os melhores, obrigado por sempre me encorajares, por todas piadas e sorrisos que tornam tudo mais fácil, nunca te poderei agradecer o suficiente por tudo que fazes por mim todos os dias, contigo a bonança chega sempre mais depressa e até a mais ingreme montanha se torna numa gentil colina. Amo-te, "my only sunshine".

STATEMENT OF INTEGRITY

I hereby declare having conducted this academic work with integrity. I confirm that I have not used plagiarism or any form of undue use of information or falsification of results along the process leading to its elaboration.

I further declare that I have fully acknowledged the Code of Ethical Conduct of the University of Minho.

Resumo

As lesões ósseas são o tipo lesões traumáticas mais comuns. O processo regenerativo do osso é um processo biológico complexo que é influenciado por vários fatores. Atualmente, os autoenxertos representam o padrão mais elevado da medicina regenerativa óssea, contudo apresentam várias desvantagens, tais como disponibilidade limitada do tecido dador ou necessidade de intervenção cirúrgica adicional para colheita do tecido dador. Assim, na área da engenharia de tecidos do osso têm-se procurado desenvolver novos sistemas artificiais que simultaneamente enderecem esta problemática e consigam mimetizar com maior precisão o tecido nativo. Neste trabalho, as excelentes propriedades regenerativas da fibroína de seda foram combinadas com nanotubos de carbono e uma matriz descelularizada derivada de células para a obtenção de novas matrizes porosas (*scaffolds*) e hierarquizadas para aplicação em abordagens da engenharia do tecido ósseo. Estes *scaffolds* foram fabricados recorrendo ao método de reticulação enzimática, modelagem através de congelamento e descelularização. A caracterização físico-química revelou que os poros do *scaffold* tinham cerca de 112 ± 22 µm e este apresentava uma porosidade total de $75 \pm 3\%$. Para além disso, observou-se que os *scaffolds* possuem um E' a rondar os 5 kPa, e que são bioativos, *in vitro*. Adicionalmente, os estudos *ex vivo* de avaliação do possível comportamento hemolítico revelaram que os *scaffolds* não possuem qualquer efeito hemolítico. Por sua vez, os estudos realizados *in vitro* envolvendo o uso de células estaminais obtidas da gordura humana (hASCs) mostraram que os *scaffolds* são capazes de suportar a proliferação celular. Para além disto, apesar do nível de atividade metabólica exibido pelas células nos *scaffolds* desenvolvidos ser semelhante aos *scaffolds* só de fibroína de seda, foi observada uma atividade da ALP superior. Por sua vez, a análise histológica mostrou que células foram capazes de migrar para o interior dos *scaffolds* e a produzir colagénio. A expressão de vários marcadores osteogénicos, tais como a ALP, OPN, Runx-2 e Col Iα, também foi observada confirmando assim o potencial osteogénico dos *scaffolds* desenvolvidos. Em suma, os *scaffolds* hierárquicos desenvolvidos neste trabalho mostraram um alto potencial para uso em abordagens da engenharia de tecido ósseo.

Palavras-chave: Engenharia de tecido ósseo, scaffolds hierárquicos, matriz descelularizada derivada de células, nanotubos de carbono, fibroína de seda

Abstract

Bone injuries are the most common traumatic injuries. The regenerative process of bone healing is a complex biological process that is influenced by several factors. The current gold standard in bone regenerative medicine are autografts which present several drawbacks, such as limited supply or donor-site morbidity. Thus, in the field of bone tissue engineering, the development of new scaffold systems that addresses the current limitations and more closely mimic the native tissue is being pursued. In this work, the excellent regenerative properties of silk fibroin were combined with carbon nanotubes and decellularized cell-derived extracellular matrix to obtain new scaffolds for bone tissue engineering applications. These easy to produce scaffolds were fabricated using enzymatic cross-liking, freeze modeling and decellularization methods. The physicochemical characterization revealed that the developed scaffolds presented pores with ≈ 112 ± 22 μm in size and a total porosity of ≈ 75 ± 3%. Furthermore, scaffolds presented an E' of ≈ 5 kPa and were bioactive *in vitro*. Additionally, *ex vivo* hemolytic assay evidenced that scaffolds expressed no hemolytic effect. Regarding biological evaluation, the cellular *in vitro* studies performed on adipose-derived stem cells (hASCs) showed that scaffolds supported cell proliferation. Besides, despite the hASCs seeded on developed scaffolds evidenced similar metabolic activity to standard silk fibroin scaffolds, they presented an increased ALP activity. Moreover, the histological stainings showed that cells were capable to migrate into the scaffolds and produce *de novo* collagen. The expression of several osteogenic markers such as ALP, OPN, Runx-2 and Col Iα was also verified, further supporting the osteogenic potential of the developed scaffolds. Overall, the hierarchical scaffolds produced in the present work show great promise for finding applications in bone tissue engineering.

Key words: Bone tissue engineering, hierarchical scaffolds, decellularized cell derived matrix, carbon nanotubes, silk fibroin

Table of Contents

List of Abbreviations

#

0D – zero dimensional

1D – one dimensional

2D – two dimensional

3D – three dimensional

A

AB – antibiotic/antimycotic

Abs – absorbance

ALP – alkaline phosphatase

B

BMP-2 – bone morphogenetic protein

BPC – biphasic calcium phosphate

BTE – bone tissue engineering

C

CDM – cell-derived extracellular matrix

cDNA – complementary DNA

Col Iα – collagen Iα

CTRL – control

D

dCDM – decellularized cell-derived extracellular matrix

DMA – dynamic mechanical analyzer

DNA – deoxyribonucleic acid

dsDNA – double strand DNA

DWCNT – double-walled carbon nanotubes

E

ECM – extracellular matrix

EDS – energy dispersive X-ray spectroscopy

F

FBS – fetal bovine serum

FN – fibronectin

G

GAGs – glycosaminoglycans

GAPDH - glyceraldehyde-3-phosphate-dehygrogenase

GelMA – gelatin methacrylate

H

h - hour

HAp – hydroxyapatite

hASC – human adipose-derived stem cells

hBMSC – human bone marrow stem cells

HE – hematoxylin and eosin staining

HPR – horseradish peroxidase

hUVEC – human umbilical vein endothelial cells

M

mg – milligram

min – minute

ml – milliliter

mm – millimeter

MWCNT – multi-walled carbon nanotubes

N

ng – nanograms

nm - nanometer

O

OPN – osteopontin

P

PBS – phosphate buffered saline

PEGDA – polyethylene (glycol) diacrylate

PG – proteoglycans

PLA – polylactic acid

PLGA – poly(lactic-co-glycolic) acid

PI – propidium iodide

Q

qRT-PCR – Real-Time Quantitative Reverse
Transcriptase-Polymerase Chain Reaction

R

rBMSC – rat bone marrow-derived mesenchymal
stem cells

RNA – ribonucleic acid

rSC – rat Schwann cells

Runx-2 – Runt-related transcription factor 2

S

SBF – simulated body fluid

SDS – sodium dodecyl sulfate

SEM – scanning electron microscopy

SF – silk fibroin

SF/dCDM – silk fibroin and decellularized cell-
derived extracellular matrix

SF/CNT – silk fibroin and carbon nanotubes

SF/dCDM/CNT – silk fibroin and decellularized
cell-derived extracellular matrix and carbon
nanotubes

SWCNT – single-walled carbon nanotubes

T

TGF – Transforming growth factor

TM – Masson's Trichrome staining

List of Figures

CHAPTER I. Introduction

CHAPTER II. Materials and Methods

CHAPTER III. Results and Discussion

List of Tables

List of Equations

CHAPTER I.

General Introduction

CHAPTER I. General Introduction

1.1. Bone

Bone is a dynamic mineralized type of tissue that serves a variety of physiological functions (1). Bones are the cornerstone of body structure as they maintain structural support and allow movement and locomotion by providing levers for muscles (2). Furthermore, it serves as protection for internal organs, stores calcium, phosphate, growth factors and cytokines, provides an environment for bone marrow production and hematopoietic cell development (1,2). Structurally, bone can be divided in two different types: the more compact cortical bone and the more porous trabecular bone (Figure 1.1). Cortical bone is dense and composes the outer part of the tissue. It possesses higher stiffness and lower toughness due to the higher mineralization content and absence of organic matter. Cortical bone is organized in concentric circles (3). The core section of the bone is composed of trabecular bone. Trabecular bone is anisotropic, highly porous and contains a sponge-like structure with interconnecting cavities (4). It is in the trabecular bone where most metabolic activity takes place. Like cortical bone, trabecular bone is also organized in concentric circles. The porosity of trabecular bone is sensitive to local cellular activity as the trabecular structures that regulate pore size can be altered by mediators of cellular activity (5). The ratio between trabecular and cortical bone varies dependent on the anatomic location (4) but overall cortical bone makes up 80% of the human skeleton, and trabecular 20% (2). In terms of composition, bone tissue is a composite of organic and inorganic phases, mainly made of collagen fibrils, calcium phosphates and a vast variety of structural proteins and polysaccharides (4,6). The collagen fibrils are mineralized by hydroxyapatite (HAp), an extremely rigid and anisotropic mineral, which is the most abundant mineral in bone and makes up for 65% of its constitution (7).
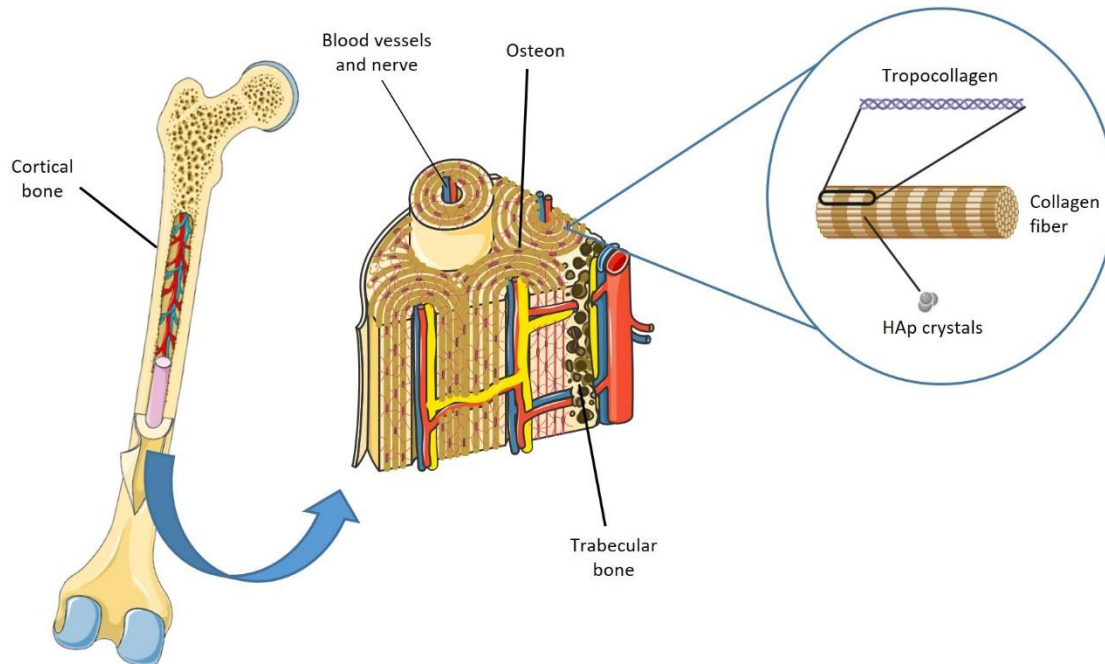
Figure 1.1 – Hierarchical structure of bone. Schematic representation of bone tissue showing compact cortical bone (outer part), porous trabecular bone (inner part) and nanostructure of bone collagen fibers.

Bone injuries are the most common traumatic injuries. The regenerative process of bone healing is a complex biological process that is influenced by the availability of blood supply, mechanical stability, size of the defect and surrounding tissue injuries. Bone healing can occur directly or indirectly. Indirect bone healing is the most common process, this is comprised by inflammatory response, bone repair and a remodeling phase. There are several chemical and cellular factors involved in the healing process. The recruitment of mesenchymal stem cells to initiate the healing cascade, collagen I and II matrix production or growth factor involvement, such as growth factor-beta (TGF-β) or bone morphogenetic protein (BMP-2), which are vital in this process (8). The current gold standard in bone regenerative medicine are autografts. These present several drawbacks like limited supply, resorption variability, donor site morbidity or high failure rate in certain sites. For these reason bone tissue engineering strategies have gained increasing interest. The development of systems that promote osteogenesis, osteoinduction, osteoconduction and osteointegration effectively is the future of bone regenerative medicine (8,9).

1.2. Bone tissue engineering

1.2.1. Current approaches for bone tissue engineering

Bone tissue engineering approaches are the next step in bone regeneration. The need for better solutions is great since the demand for bone grafts to treat injuries or pathologies is high. Most bone tissue engineering approaches combine cells, specific culture conditions and biomaterial scaffolds with biochemical and physical stimuli to achieve *in vitro* bone formation. At the moment, the existing and most used approaches are not patient specific nor biochemically specific. Long term implants are also very limited for many applications, because of overtime stress shielding and implant loosening (10). Long term repair and favorable clinical outcome by using responsive biomaterials capable of adaptation to the dynamic physiological and mechanical *in vivo* environments is still a major challenge in bone tissue engineering (11).

Currently, scaffolds that can provide mechanical support while modulating the healing process represent the ideal regenerative bone therapy (12). Biomimetic three dimensional (3D) scaffolds that mimic the physical and chemical properties of the native tissue extracellular matrix (ECM) are considered the ideal substitutes for autologous bone grafts (13).

1.2.2. Hierarchical scaffolds

Bone tissue engineering heavily relies on the development of scaffolds for effective bone defect reparation. Optimal scaffolds should possess osteoinductivity, facilitate cell attachment, proliferation and migration. Scaffolds play a crucial role in bone tissue engineering by providing a 3D environment for cell adhesion and proliferation (14). Mimicking the native tissue in its hierarchical structure, chemical composition and properties is the ultimate goal of regenerative scaffold designing. In bone tissue engineering, the strife for ever more biomimetic scaffold systems has led to use biomotifs in scaffold design, attempting to recreate bone matrix structure and composition (15). There are several different approaches and targets for biomimicry, ranging from introduction of molecules at the nano scale to the micro and macro structure of scaffolds. An example of this is the structural mimicking of Harvesian bone as seen in the work of Zhang *et al.* (16). In this work, inspired by the hierarchical structure and function of bone, a 3D printed biomimetic

bone scaffold was developed. With this approach, mimicry of Haversian canals, Volkmann canals and cancellous bone was achieved also combining a high control over the properties of these bone-mimicking structures and multicellular spatial distribution. Osteogenic and angiogenic gene expression analysis of co-cultured human bone marrow stem cells (hBMSCs) and human umbilical vein endothelial cells (hUVECs) showed an increase of these markers when seeded onto the scaffolds. Similarly, when co-culturing rat bone marrow–derived mesenchymal stem cells (rBMSC) and rat Schwann cells (rSC) onto the developed scaffolds, the proliferation and expression of neurotrophic factors was verified. Evidencing the potential of this hierarchical system for osteogenic, angiogenic and neurogenic differentiation. Which is substantiated by the *in vivo* assay where rapid new bone formation and accelerated ingrowth of blood vessels was observed (16). Another approach for the development of biomimetic scaffolds consists in the biomimicry of the chemical composition of bone. Zhou *et al*. (17) developed 3D printed scaffolds with hierarchical biomimetic structure for osteochondral regeneration. In this work, poly (lactic-co-glycolic) acid (PLGA) nanoparticles were used to encapsulate transforming growth factor-beta (TGF-β1). These nanoparticles with encapsulated TGF-β1 were produced via the co-axial electrospraying method, while a stereolithography-based 3D printer was used to create the scaffold of gelatin methacrylate (GelMA) and polyethylene (glycol) diacrylate (PEGDA). Both the PLGA nanoparticles and nano hydroxyapatite were incorporated into the upper and lower layer of the scaffold. By using this approach, the authors were able to release TGF-β1 in a controlled manner, emulating the bone microenvironment. That interesting scaffold design successfully upregulated the expression of osteogenesis-associated genes. The results evidenced the osteogenic differentiation potential of this system, which was further confirmed by histological staining of calcium deposits with Alizarin red (17).

Overall the complex structure of bone tissue requires a multidimensional approach that takes into account multiple structural and biological factors. Hence, to more closely mimic the natural tissue and provide better solutions for bone lesions, an increase in complexity and effectiveness of scaffolds is necessary.

There is a vast variety of materials with different properties used to produce scaffolds for bone tissue. Calcium phosphates such as HAp or tricalcium phosphate are the most commonly used bioactive inorganic materials for making ceramic scaffolds. These types of scaffolds are highly biocompatible and osteoconductive due to similarities between their chemical composition and natural bone composition (18,19). Furthermore, HAp scaffolds are capable of osteointegration through chemical bonding and inducing bone tissue formation all while exhibiting controlled degradation rate (20). The major problem concerning

ceramic scaffolds is the brittle nature, low mechanical stress resistance compared with bone (21) and poor fidelity of these materials. Hydrogels due their inherent biomimetic structure, ability to incorporate biomolecules, controlled degradability, intrinsic cytocompatibility and versatility are a promising formulation for bone tissue engineering application. The ability to control the stiffness and structure to more precisely mimic complex tissues makes hydrogels optimal scaffolds with increased functionality (22). Furthermore, hydrogels are cost effective and can incorporate nanoparticles, biological factors or cells to create modified hydrogels that can serve as delivery vessels for pharmaceuticals, antibodies, nucleic acids, growth factors and stem cells (23–27).

Nanocomposite scaffolds are a combination of organic and inorganic components to try to mimic the organization of natural ECM. Nanocomposites can be produced through many different methodologies such as composite formation with nanomaterials, molecular self-assembly or electrospinning (28–30). These scaffolds have shown to regulatory affect cell adhesion, migration, proliferation, genetic expression, among other osteoblast's and bone derived stem-cells' behavior aspects (31–34). Research in this area is mainly focused on new nanoscale elements that could more effectively provide structural and mechanical advantages to the bone while directly influencing cellular behavior.

1.2.2.1. Multi-walled carbon nanotubes

Another interesting approach is the use of carbon for nanoparticle development. The unique and versatile properties of carbon have made it an ideal candidate for the development of new bone tissue engineering strategies. Carbon can be processed in several different dimensions, from 3D graphite, two-dimensional (2D) graphene, one-dimensional (1D) carbon nanotubes to zero-dimensional (0D) carbon dots or carbon nanodiamonds (35). The most used iteration of carbon nanoparticles is carbon nanotubes, namely single-walled carbon nanotubes (SWCNT), double-walled carbon nanotubes (DWCNT) or multi-walled carbon nanotubes (MWCNT) (Figure 1.2), according to the number of layers constituting their structure (36). These nanotubes possess good strength, elasticity, and fatigue resistance and can be used to improve the overall mechanical properties of constructs. Their high affinity for cell binding proteins can promote stem cell differentiation and their electrical conductivity can be controlled by adjusting size and diameter (37,38). The carbon nanotubes' unique electrical conductivity has gained increasing interest in bone tissue engineering. Electrical stimulation can accelerate bone formation, regeneration, ECM protein synthesis, and enhance

osteogenic markers expression (39). Compared to the other two forms, MWCNTs possess higher structural stability due to its multi-layered architecture. On the other hand, the various concentric layers confer the material with higher rigidity and a fiber-like shape that may increase physical destructiveness (36). Another important advantage of carbon nanotubes is that their micrometer length and nanometer diameter resembles constituents of ECM of connective tissue such as collagen fibrils (40). With this in mind, Świętek *et al.* (40) used hydroxylated MWCNTs in combination with magnetic iron oxide nanoparticles incorporated into a porous PCL matrix to create a multi-functional system that enables multi-way cell stimulation. These hybrid nanoparticles were synthesized by co-precipitation, and the solvent casting/porogen leaching method was used to fabricate the scaffolds. This preliminary research developed with an osteoblastic cell line showed that the carbon nanotubes had a positive effect on cell adhesion (40).

Despite the recent leap in bone tissue engineering approaches, the biomimicry of the natural tissue and its ECM in its architecture and composition is still the ultimate goal for bone regenerative systems. Furthermore, the theoretically best available materials for tissue regeneration applications are still natural derived. The ability to directly use components that are naturally present in the ECM is an advantage to mimic specific aspects of this tissue (41). Currently, collagen, glycosaminoglycans, chitosan, silk fibroin and elastin are the most widely used naturally derived polymers for tissue engineering applications (42–44). These natural polymers often possess low mechanical properties. Therefore, the combination of two or more polymers can be used to further biomimicry with the ultimate goal of creating more effective, viable and versatile scaffold.
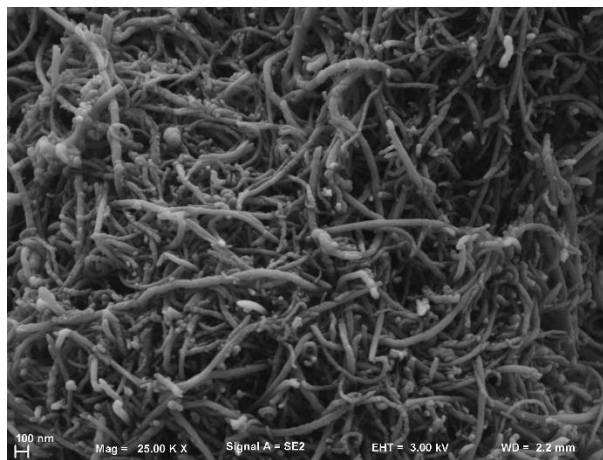
Figure 1.2 – Representative image of multi-walled carbon nanotubes. Multi-walled carbon nanotubes imaged using scanning electron microscopy (scale bar = 100 nm).

1.2.2.2. Silk Fibroin

Silk fibroin (SF) is a hydrophobic structural protein most commonly obtained from *Bombyx mori* that comprises an equimolar ratio of a heavy hydrophobic chain and a light relatively hydrophilic chain (Figure 1.3) (45,46). Silk fibroin molecular structure possesses the necessary phenol groups in the tyrosine side chains for enzymatic cross-linking, a process used to bind polymeric chains and thus improve polymers properties (47,48).
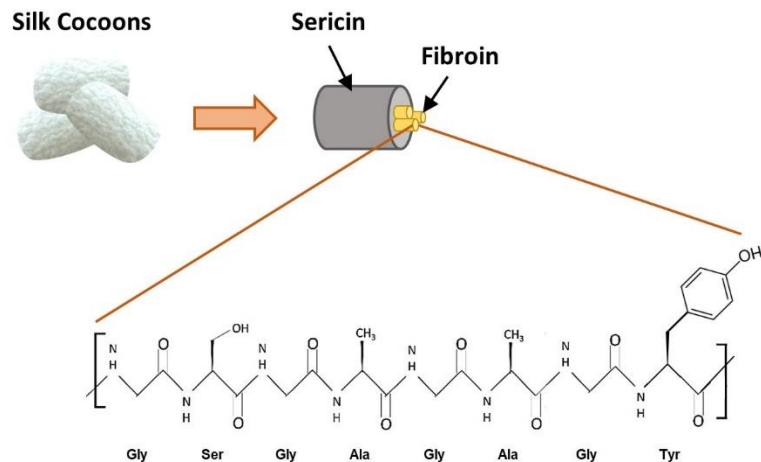
Figure 1.3 – Silk composition. Representation of silk obtained from silkworm cocoon, showing sericin and fibroin and fibroin's molecular composition.

Its unique mechanical properties make it a versatile tool for multiple applications. In the case of scaffold production, this biopolymer presents specific advantages in both versatility and mechanical strength. SF porosity can be controlled through ice-templating allowing the production of anisotropic or hierarchical structures (49). The ability to use several processing techniques to obtain a vast array of morphologies and scaffold types, from nanoparticles to hydrogels, is another great advantage of SF (50). More specifically the SF structure similarity to the native structure of collagen type I combined with its excellent mechanical properties, slow degradation rate, and high morphology control makes it an extremely versatile material for bone tissue engineering applications (46). Moreover, SF can be used in a vast array of applications such as load-bearing scaffolds or sutures, taking advantage of the SF flexibility and high tensile strength (50). Also, its mechanical strength is superior when compared to other biodegradable polymers, like collagen or chitosan,

and its proteolytical degradation presents an advantage when compared to synthetic polymers (51). The usefulness of these characteristics prompted Liu *et al.* (52) to develop a biomimetic porous SF/biphasic calcium phosphate (BCP) scaffold with improved mechanical properties, using phase separation method and freeze-drying. In fact, the results showed that the addition of SF improved scaffolds' mechanical properties when compared to pure BCP scaffolds and improved pre-osteoblasts cells growth. That system demonstrated to mimic the natural bone matrix and to display excellent osteogenic capacity in a rat model, as evidenced by the rapid proliferation of seeded osteoblasts and the increased alkaline phosphatase (ALP) activity. Furthermore, the possibility to form an apatite layer through the exchange of calcium and phosphorous between BCP and body fluids, may provide osteoblast with the necessary elements to secrete bone matrix (52).

The ECM plays an important role in native bone tissue, it provides a structural platform for cell adhesion and its components also regulate cell behavior. Being part of the natural bone tissue, it stands clear that the use the ECM for production of scaffolds would provide huge advantages in respect to the mimetic ability, and ultimately consist the best possible raw material for scaffolds development.

1.3. ECM

In order to achieve critical biophysical and biochemical support, cells produce and secrete ECM. The ECM is a network of well-organized non-cellular components that provide not only structural support but also cellular regulation (53).

Fibrous-forming proteins like collagens, especially collagen type I and II, elastin, fibronectin (FN), laminins, proteoglycans (PGs), glycosaminoglycans (GAGs) and other glycoproteins are the main constituents of the ECM. Different chemokines, cytokines and growth factors are bond to specific ECM molecules and can be released according to the physiological needs of the cell (54). In terms of structure, the ECM tends to form a complex matrix network composed of large fibrillar structures that are connected with ECM molecules. Among its component's collagen is the most abundant protein in the ECM and alongside laminin and FN confers structural resistance. GAGs are one of the main biomolecules in the ECM. Along PGs they fill most of the empty spaces in the matrix. The negative charges and their high-density lead to high osmotic swelling

pressure, making them ideal space fillers, a trait shared with PGs. They are also involved in cell proliferation, cell migration and cell-to-cell and cell-to-matrix interactions (55,56). As mentioned above, PGs are also vital for the structure and functionality of the ECM. They participate in several important cellular processes like cell adhesion, apoptosis, differentiation, migration, proliferation and signaling (57).

In bone, the ECM plays a vital role in the remodeling process. In this sense, the ECM of the various bone tissue compartments play an important role managing bone remodeling by the interplay activity of osteoblast and osteoclasts. Furthermore, the ECM acts as natural scaffold since it supports mineral deposition and confers flexibility to what would be an overly rigid tissue. The cell matrix is also responsible for regulating cell activity as it influences both osteoclast and osteoblast lineages and the differentiation of mesenchymal stem cells to become osteoblasts (58).

The natural properties and proteins of the ECM can be extracted from tissues and organs or from cellular monolayers using decellularization protocols. Decellularization prevents the occurrence of an immunological response and as such is of great importance for further application of the ECM. That procedure consisted of the removal of cellular content and genetic material without significantly compromising the ECM structure and composition. The use of appropriate protocols to minimize the damage to the ECM is very important. Essentially every decellularization protocol consists of a way to lyse cells and subsequent washing to remove the resultant cellular content and genetic material. There are a vast array of protocols that can be used to decellularize ECM, these agents can be categorized in chemical, physical and biological methods (59).

The use of chemical agents is one of the most commonly used means of decellularization (60). These include acids and bases, hypotonic and non-hypotonic solutions, alcohols, surfactants and solvents. Surfactants are the most commonly used chemical agents and work lysing cells through the disarranging of the phospholipid cell membrane (61). Within the surfactants sodium dodecyl sulfate (SDS) and Triton X-100 are among the most widely used.

Physical agents are frequently used in combination with chemical or biological methods and are effective decellularization agents that can reduce the use of chemical reagents. Agitation, sonication, mechanical pressure or freeze-thaw cycles are the most common treatments used and allow for disruption

of cell membranes, detachment of cells from the ECM network and further rinsing to remove cell remnants (62).

Regarding biological agents, enzymes are the most commonly used agents. Enzymes figuring in decellularization protocols include nucleases, trypsin, collagenase, lipase, dispase, thermoslysin and α-galactosidase (63). Those components possess a high specificity and can be employed to target nucleic acid remnants after cell fraction or peptide bonds that bind the cell to its ECM (63,64). Despite this, achieving decellularization with enzymatic treatment alone is difficult and enzyme residue can provoke an immune response or hinder recellularization (63).

The appropriate strategy to tackle the decellularization of a certain tissue or cellular monolayer highly depends on the characteristics of it. Nevertheless most decellularization protocols employ a combination physical, chemical and biological agents to achieve optimal results, this emphasizes that decellularization has to be tailored to achieve best results (65). Taking advantage of the specific properties each method has to offer is a step forward in the development of improved decellularization protocols that more closely preserve the ECM composition and structure.

1.3.1. Cell derived Extracellular matrix

Regarding the production of cell derived extracellular matrix (CDM), the cell source determines the ECM composition, being that CDM compositions for the most part resemble the cells from where they were obtained (66). Furthermore, CDM have been produced using both primary cells and cell lines (Figure 1.4).
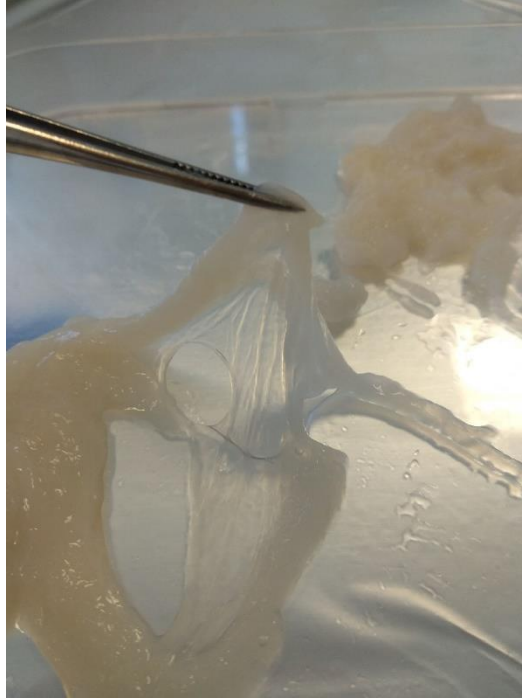
Figure 1.4 – Cell-derived extracellular matrix. Image of cell-derived extracellular matrix (CDM) obtained from hASCs culture.

Primary cells directly harvested without passaging are usually considered the ideal cell source due to their close resemblance to the *in vivo* phenotype (66). CDM can be derived from autologous cells, allow for an easier pathogen elimination and can be created using patient-specific cells (67). Their high availability and high degree of customization is also a major advantage. The use of CDMs allows for control over parameters like cell types, culture systems or external stimuli (66). Despite this, its weak mechanical properties poses an issue for its application in *in vivo* studies (68). Matrices can be engineered by introducing soluble factors, proteins of interest or co-culturing different cell types before decellularization (69). Taking advantage of CDM high availability and easy access Savitri *et al.* (70) used four different CDM obtained from four different cell types to assess their effect on macrophage behavior and wound healing. In this study, human lung fibroblasts, hBMSCs, human dermal fibroblasts and human umbilical cord-blood mesenchymal stem cells were cultured for seven days. The subsequent decellularized matrices were then characterized for their composition (70). This showcases the utility of CDMs allowing for fast and specific production of decellularized CDMs (dCDM). Furthermore, the study of Noh *et al.* (71) illustrates the potential of CDM for scaffold fabrication. They used CDM with high amounts of collagen type I to coat PLGA/ polylactic acid (PLA)

scaffolds with the goal to mimic an osteogenic microenvironment. Collagen type I-overexpression cell line was cultured for 4 days and then submitted to a brief decellularization process using Triton X-100, NH$_4$OH, DNase and RNase. The obtained matrices were then transferred into tubes, forming an aqueous suspension in which the scaffolds were immersed and incubated. Human umbilical cord blood mesenchymal stem cells were seeded onto three different types of scaffolds: CDM-coated scaffolds, plain polymer scaffolds as control group and fibronectin coated polymer scaffolds. All scaffolds were placed in medium with osteogenic supplementation. By analyzing the ALP activity and osteogenic gene expression it was shown that CDM-coated scaffolds support osteogenic differentiation better than both plain polymer scaffolds and fibronectin-coated scaffolds. This verifies the ability of this system to produce an optimal biomimetic 3D microenvironment for cell differentiation even when compared with commonly used biomaterials derived from natural sources (71).

The use of dCDMs for scaffold fabrication is still in its early stages. However, this interesting technology will certainly be vastly explored in the future and shows great promise for tissue engineering.

1.4. References

1.   Grabowski P. Physiology of Bone. Endocr Dev. 2015;28:33–55.

2.   Clarke B. Normal bone anatomy and physiology. Clin J Am Soc Nephrol. 2008 Nov;3 Suppl 3(Suppl 3):S131-9.

3.   Zimmermann EA, Ritchie RO. Bone as a Structural Material. Adv Healthc Mater. 2015 Jun;4(9):1287–304.

4.   Lopes D, Martins-Cruz C, Oliveira MB, Mano JF. Bone physiology as inspiration for tissue regenerative therapies. Biomaterials. 2018 Dec;185:240–75.

5.   Wubneh A, Tsekoura EK, Ayranci C, Uludağ H. Current state of fabrication technologies and materials for bone tissue engineering. Acta Biomater. 2018 Oct;80:1–30.

6.   Perić Kačarević Ž, Rider P, Alkildani S, Retnasingh S, Pejakić M, Schnettler R, et al. An introduction to bone tissue engineering. Int J Artif Organs. 2020 Feb;43(2):69–86.

7.   Lowe B, Hardy JG, Walsh LJ. Optimizing Nanohydroxyapatite Nanocomposites for Bone Tissue Engineering. ACS omega. 2019 Dec 18;5(1):1–9.

8.   Pereira HF, Cengiz IF, Silva FS, Reis RL, Oliveira JM. Scaffolds and coatings for bone regeneration. J Mater Sci Mater Med. 2020 Mar;31(3):27.

9.   Roseti L, Parisi V, Petretta M, Cavallo C, Desando G, Bartolotti I, et al. Scaffolds for Bone Tissue Engineering: State of the art and new perspectives. Mater Sci Eng C Mater Biol Appl. 2017 Sep;78:1246–62.

10.   Hirata Y, Inaba Y, Kobayashi N, Ike H, Fujimaki H, Saito T. Comparison of Mechanical Stress and Change in Bone Mineral Density Between Two Types of Femoral Implant Using Finite Element Analysis. J Arthroplasty. 2013;28(10):1731–5.

11.   Bagde AD, Kuthe AM, Quazi S, Gupta V, Jaiswal S, Jyothilal S, et al. State of the Art Technology for Bone Tissue Engineering and Drug Delivery. IRBM. 2019;40(3):133–44.

12.   Rahimnejad M, Derakhshanfar S, Zhong W. Biomaterials and tissue engineering for scar management in wound care. Burn trauma. 2017 Jan 21;5:4.

13.   Kim J-W, Han Y-S, Lee H-M, Kim J-K, Kim Y-J. Effect of Morphological Characteristics and Biomineralization of 3D-Printed Gelatin/Hyaluronic Acid/Hydroxyapatite Composite Scaffolds on Bone Tissue Regeneration. Int J Mol Sci. 2021 Jun;22(13).

14.   Ma H, Feng C, Chang J, Wu C. 3D-printed bioceramic scaffolds: From bone tissue engineering to tumor therapy. Acta Biomater. 2018;79:37–59.

15.   Du Y, Guo JL, Wang J, Mikos AG, Zhang S. Hierarchically designed bone scaffolds: From internal cues to external stimuli. Biomaterials. 2019/07/03. 2019 Oct;218:119334.

16.   Zhang M, Lin R, Wang X, Xue J, Deng C, Feng C, et al. 3D printing of Haversian bone-mimicking

scaffolds for multicellular delivery in bone regeneration. Sci Adv. 2020 Mar 20;6(12):eaaz6725–eaaz6725.

17. Zhou X, Esworthy T, Lee S-J, Miao S, Cui H, Plesiniak M, et al. 3D Printed scaffolds with hierarchical biomimetic structure for osteochondral regeneration. Nanomedicine. 2019 Jul;19:58–70.

18. Ko C-L, Chen W-C, Chen J-C, Wang Y-H, Shih C-J, Tyan Y-C, et al. Properties of osteoconductive biomaterials: Calcium phosphate cement with different ratios of platelet-rich plasma as identifiers. Mater Sci Eng C. 2013;33(6):3537–44.

19. LeGeros RZ. Calcium Phosphate-Based Osteoinductive Materials. Chem Rev. 2008 Nov 12;108(11):4742–53.

20. Cambra-Moo O, Nacarino Meneses C, Rodríguez Barbero MÁ, García Gil O, Rascón Pérez J, Rello-Varona S, et al. An approach to the histomorphological and histochemical variations of the humerus cortical bone through human ontogeny. J Anat. 2014 Jun 1;224(6):634–46.

21. Gao C, Deng Y, Feng P, Mao Z, Li P, Yang B, et al. Current progress in bioactive ceramic scaffolds for bone repair and regeneration. Int J Mol Sci. 2014 Mar 18;15(3):4714–32.

22. Nejadnik MR, Yang X, Bongio M, Alghamdi HS, van den Beucken JJJP, Huysmans MC, et al. Self-healing hybrid nanocomposites consisting of bisphosphonated hyaluronan and calcium phosphate nanoparticles. Biomaterials. 2014;35(25):6918–29.

23. Hokugo A, Saito T, Li A, Sato K, Tabata Y, Jarrahy R. Stimulation of bone regeneration following the controlled release of water-insoluble oxysterol from biodegradable hydrogel. Biomaterials. 2014;35(21):5565–71.

24. Ansari S, Moshaverinia A, Pi SH, Han A, Abdelhamid AI, Zadeh HH. Functionalization of scaffolds with chimeric anti-BMP-2 monoclonal antibodies for osseous regeneration. Biomaterials. 2013/09/19. 2013 Dec;34(38):10191–8.

25. Bae MS, Ohe J-Y, Lee JB, Heo DN, Byun W, Bae H, et al. Photo-cured hyaluronic acid-based hydrogels containing growth and differentiation factor 5 (GDF-5) for bone tissue regeneration. Bone. 2014;59:189–98.

26. Hoffman MD, Van Hove AH, Benoit DSW. Degradable hydrogels for spatiotemporal control of mesenchymal stem cells localized at decellularized bone allografts. Acta Biomater. 2014;10(8):3431–41.

27. Komatsu K, Shibata T, Shimada A, Ideno H, Nakashima K, Tabata Y, et al. Cationized gelatin hydrogels mixed with plasmid DNA induce stronger and more sustained gene expression than atelocollagen at calvarial bone defects in vivo. J Biomater Sci Polym Ed. 2016 Mar 23;27(5):419–30.

28. Pant HR, Risal P, Park CH, Tijing LD, Jeong YJ, Kim CS. Synthesis, characterization, and mineralization of polyamide-6/calcium lactate composite nanofibers for bone tissue engineering. Colloids Surfaces B Biointerfaces. 2013;102:152–7.

29. Lee SS, Hsu EL, Mendoza M, Ghodasra J, Nickoli MS, Ashtekar A, et al. Gel scaffolds of BMP-2-

binding peptide amphiphile nanofibers for spinal arthrodesis. Adv Healthc Mater. 2014/04/22. 2015 Jan 7;4(1):131–41.

30. Singh MK, Gracio J, LeDuc P, Gonçalves PP, Marques PAAP, Gonçalves G, et al. Integrated biomimetic carbon nanotube composites for in vivo systems. Nanoscale. 2010;2(12):2855–63.

31. Biggs MJP, Richards RG, Gadegaard N, Wilkinson CDW, Dalby MJ. Regulation of implant surface cell adhesion: characterization and quantification of S-phase primary osteoblast adhesions on biomimetic nanoscale substrates. J Orthop Res. 2007 Feb 1;25(2):273–82.

32. Lamers E, Domanski M, Luttge R, Figdor CG, Walboomers XF, Jansen JA, et al. DYNAMIC CELL ADHESION AND MIGRATION ON NANOSCALE. 2012;182–94.

33. Hu J, Zhou Y, Huang L, Liu J, Lu H. Effect of nano-hydroxyapatite coating on the osteoinductivity of porous biphasic calcium phosphate ceramics. BMC Musculoskelet Disord. 2014 Apr 1;15:114.

34. Kantawong F, Burgess KE V, Jayawardena K, Hart A, Burchmore RJ, Gadegaard N, et al. Whole proteome analysis of osteoprogenitor differentiation induced by disordered nanotopography and mediated by ERK signalling. Biomaterials. 2009;30(27):4723–31.

35. Peng Z, Zhao T, Zhou Y, Li S, Li J, Leblanc RM. Bone Tissue Engineering via Carbon-Based Nanomaterials. Adv Healthc Mater. 2020 Mar 1;9(5):1901495.

36. Li Y, Cao J. The impact of multi-walled carbon nanotubes (MWCNTs) on macrophages: contribution of MWCNT characteristics. Sci China Life Sci. 2018 Nov;61(11):1333–51.

37. Pei B, Wang W, Dunne N, Li X. Applications of Carbon Nanotubes in Bone Tissue Regeneration and Engineering: Superiority, Concerns, Current Advancements, and Prospects. Nanomater (Basel, Switzerland). 2019 Oct;9(10).

38. Eivazzadeh-Keihan R, Maleki A, de la Guardia M, Bani MS, Chenab KK, Pashazadeh-Panahi P, et al. Carbon based nanomaterials for tissue engineering of bone: Building new bone on small black scaffolds: A review. J Adv Res. 2019 Jul;18:185–201.

39. Gholizadeh S, Moztarzadeh F, Haghighipour N, Ghazizadeh L, Baghbani F, Shokrgozar MA, et al. Preparation and characterization of novel functionalized multiwalled carbon nanotubes/chitosan/β-Glycerophosphate scaffolds for bone tissue engineering. Int J Biol Macromol. 2017;97:365–72.

40. Świętek M, Brož A, Tarasiuk J, Wroński S, Tokarz W, Kozieł A, et al. Carbon nanotube/iron oxide hybrid particles and their PCL-based 3D composites for potential bone regeneration. Mater Sci Eng C Mater Biol Appl. 2019 Nov;104:109913.

41. Hubbell JA. Materials as morphogenetic guides in tissue engineering. Curr Opin Biotechnol. 2003;14(5):551–8.

42. Saber-Samandari S, Saber-Samandari S. Biocompatible nanocomposite scaffolds based on copolymer-grafted chitosan for bone tissue engineering with drug delivery capability. Mater Sci Eng C. 2017;75:721–32.

43. Sommer MR, Vetsch JR, Leemann J, Müller R, Studart AR, Hofmann S. Silk fibroin scaffolds with inverse opal structure for bone tissue engineering. J Biomed Mater Res Part B Appl Biomater. 2017

Oct 1;105(7):2074–84.

44.   Mizutani N, Kageyama S, Yamada M, Hasegawa M, Miyamoto K, Horiuchi T. The behavior of ligament cells cultured on elastin and collagen scaffolds. J Artif Organs. 2014;17(1):50–9.

45.   Singh BN, Panda NN, Mund R, Pramanik K. Carboxymethyl cellulose enables silk fibroin nanofibrous scaffold with enhanced biomimetic potential for bone tissue engineering application. Carbohydr Polym. 2016;151:335–47.

46.   Bhattacharjee P, Kundu B, Naskar D, Kim H-W, Maiti TK, Bhattacharya D, et al. Silk scaffolds in bone tissue engineering: An overview. Acta Biomater. 2017 Nov;63:1–17.

47.   Partlow BP, Hanna CW, Rnjak-Kovacina J, Moreau JE, Applegate MB, Burke KA, et al. Highly tunable elastomeric silk biomaterials. Adv Funct Mater. 2014 Aug;24(29):4615–24.

48.   Grabska-Zielińska S, Sionkowska A. How to Improve Physico-Chemical Properties of Silk Fibroin Materials for Biomedical Applications?-Blending and Cross-Linking of Silk Fibroin-A Review. Mater (Basel, Switzerland). 2021 Mar;14(6).

49.   Wen J, Yao J, Chen X, Shao Z. Silk Fibroin Acts as a Self-Emulsifier to Prepare Hierarchically Porous Silk Fibroin Scaffolds through Emulsion-Ice Dual Templates. ACS omega. 2018 Mar;3(3):3396–405.

50.   Melke J, Midha S, Ghosh S, Ito K, Hofmann S. Silk fibroin as biomaterial for bone tissue engineering. Acta Biomater. 2016;31:1–16.

51.   Mottaghitalab F, Hosseinkhani H, Shokrgozar MA, Mao C, Yang M, Farokhi M. Silk as a potential candidate for bone tissue engineering. J Control Release. 2015;215:112–28.

52.   Liu B, Gao X, Sun Z, Fang Q, Geng X, Zhang H, et al. Biomimetic porous silk fibroin/biphasic calcium phosphate scaffold for bone tissue regeneration. J Mater Sci Mater Med. 2018 Dec;30(1):4.

53.   Theocharis AD, Skandalis SS, Gialeli C, Karamanos NK. Extracellular matrix structure. Adv Drug Deliv Rev. 2016 Feb;97:4–27.

54.   Rozario T, DeSimone DW. The extracellular matrix in development and morphogenesis: a dynamic view. Dev Biol. 2010 May;341(1):126–40.

55.   Yi S, Ding F, Gong L, Gu X. Extracellular Matrix Scaffolds for Tissue Engineering and Regenerative Medicine. Curr Stem Cell Res Ther. 2017;12(3):233–46.

56.   Richter RP, Baranova NS, Day AJ, Kwok JC. Glycosaminoglycans in extracellular matrix organisation: are concepts from soft matter physics key to understanding the formation of perineuronal nets? Curr Opin Struct Biol. 2018 Jun;50:65–74.

57.   Iozzo R V, Schaefer L. Proteoglycan form and function: A comprehensive nomenclature of proteoglycans. Matrix Biol. 2015 Mar;42:11–55.

58.   Alford AI, Kozloff KM, Hankenson KD. Extracellular matrix networks in bone remodeling. Int J Biochem Cell Biol. 2015;65:20–31.

59.   Choudhury D, Yee M, Sheng ZLJ, Amirul A, Naing MW. Decellularization systems and devices: State-of-the-art. Acta Biomater. 2020;115:51–9.

60.   McCrary MW, Vaughn NE, Hlavac N, Song YH, Wachs RA, Schmidt CE. Novel Sodium Deoxycholate-Based Chemical Decellularization Method for Peripheral Nerve. Tissue Eng Part C Methods. 2020 Jan;26(1):23–36.

61.   Gilpin A, Yang Y. Decellularization Strategies for Regenerative Medicine: From Processing Techniques to Applications. Biomed Res Int. 2017;2017:9831534.

62.   Roth SP, Glauche SM, Plenge A, Erbe I, Heller S, Burk J. Automated freeze-thaw cycles for decellularization of tendon tissue - a pilot study. BMC Biotechnol. 2017 Feb 14;17(1):13.

63.   Crapo PM, Gilbert TW, Badylak SF. An overview of tissue and whole organ decellularization processes. Biomaterials. 2011;32(12):3233–43.

64.   Somuncu ÖS. Decellularization Concept in Regenerative Medicine. Adv Exp Med Biol. 2020;1212:71–85.

65.   Keane TJ, Swinehart IT, Badylak SF. Methods of tissue decellularization used for preparation of biologic scaffolds and in vivo relevance. Methods. 2015;84:25–34.

66.   Fitzpatrick LE, McDevitt TC. Cell-derived matrices for tissue engineering and regenerative medicine applications. Biomater Sci. 2015 Jan;3(1):12–24.

67.   Carvalho MS, Silva JC, Cabral JMS, da Silva CL, Vashishth D. Cultured cell-derived extracellular matrices to enhance the osteogenic differentiation and angiogenic properties of human mesenchymal stem/stromal cells. J Tissue Eng Regen Med. 2019 Sep 1;13(9):1544–58.

68.   Kim IG, Hwang MP, Park JS, Kim S-H, Kim J-H, Kang HJ, et al. Stretchable ECM Patch Enhances Stem Cell Delivery for Post-MI Cardiovascular Repair. Adv Healthc Mater. 2019 Sep 1;8(17):1900593.

69.   Harris GM, Raitman I, Schwarzbauer JE. Cell-derived decellularized extracellular matrices. Methods Cell Biol. 2017/11/02. 2018;143:97–114.

70.   Savitri C, Ha SS, Liao E, Du P, Park K. Extracellular matrices derived from different cell sources and their effect on macrophage behavior and wound healing. J Mater Chem B. 2020 Nov;8(42):9744–55.

71.   Noh YK, Du P, Kim IG, Ko J, Kim SW, Park K. Polymer mesh scaffold combined with cell-derived ECM for osteogenesis of human mesenchymal stem cells. Biomater Res. 2016;20(1):6.

CHAPTER II.

Materials and Methods

CHAPTER II. Materials and Methods

2.1. Materials and methods

2.1.1. Scaffold's production and characterization

2.1.1.1. Silk fibroin solution preparation

Purified SF was prepared by removing the sericin protein from the cocoons in a 0.02 M boiling sodium carbonate solution for 1 h, followed by a 30 min wash with boiling distilled water to completely remove the degumming solution. The obtained SF was dissolved in a 9.3 M lithium bromide (Sigma Aldrich, USA) solution for 1 h at 70°C, and dialyzed in distilled water for 48 h using the benzoylated dialysis tubing (MWCO: 2 kDa) (Sigma Aldrich, USA). SF was concentrated against a 20 wt% poly (ethylene glycol) (Sigma Aldrich, USA) solution for at least 6 h. The final concentration of SF was determined by measuring the dry weight of the SF solution placed in the oven at 70°C overnight. Meanwhile, the prepared SF solution was stored at 4°C until further use (Figure 2.1).
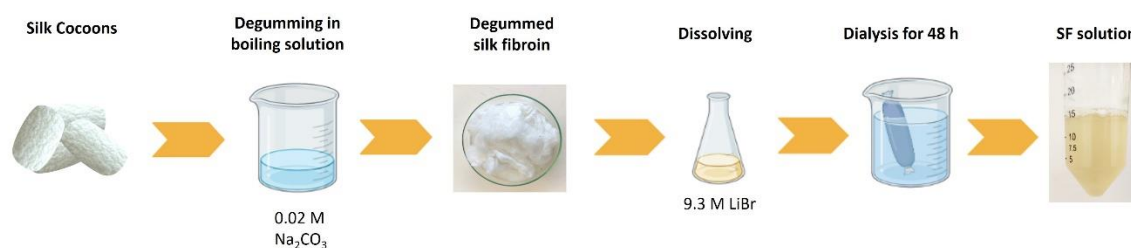

Figure 2.1 – Silk fibroin production. Schematic representation of silk fibroin production showing the degumming of silk fibroin followed by dissolution of obtained material with lithium bromide, and lastly, the submission of the dissolved material to dialysis.

2.1.1.2. Cell-derived ECM production

Human adipose-derived stem cells (hASCs) were isolated from the lipoaspirate samples obtained under a protocol previously established with the Department of Plastic Surgery of Hospital da Prelada (Porto, Portugal), and under subject's informed consent. Next, 3,000 cells per cm^2 were seeded into a 150 cm^2 T-flask in α-MEM medium (Gibco, USA) supplemented with 10% fetal bovine serum (FBS) (Gibco, USA) and 1% antibiotic/antimycotic (AB) (Gibco, USA), and maintained at 37°C under a humidified atmosphere of 5% v/v CO_2 in air. The medium was changed twice a week until cells reached 80% of confluence. Afterward, hASCs were subcultured at an initial cell density of 3,000 cells per cm^2 in a 150 cm^2 T-flask and kept under α-MEM medium supplemented with 0.05 mM ascorbic acid, 10 mM β-Glycerophosphate, 100 nM dexamethasone (Sigma Aldrich, USA), 10% FBS and 1% AB. Cells were cultured for 6 weeks under a humidified atmosphere of 5% v/v CO_2 in air and medium was changed twice a week in order to produce a condensed cell monolayer with high amounts of ECM.

2.1.1.3. Decellularization

The decellularization was performed as described in Maia *et al.* (1). Briefly, previously obtained condensed cell monolayers were subjected to six cycles of freeze at -80°C for 12 h followed by thawing at 37°C until completely defrost. Afterwards, condensed cell monolayers were cut into smaller pieces with ≈ 3 mm. Then, they were incubated in a solution of 2% (v/v) Triton X-100 (Sigma Aldrich, USA) with 10% (v/v) AB for 24 h at 4°C under 200 rpm. To remove Triton X-100 solution, monolayers were centrifuged at 5,000 rpm for 5 min at 4°C and the supernatant was discarded. The samples were vortexed and incubated in 0.1% (w/v) of SDS (Sigma Aldrich, USA) with 10% (v/v) AB for 48 h at 4°C under 200 rpm. Condensed cell monolayers were centrifuged at 5,000 rpm for 5 min at 4°C and the supernatant was discarded. Again, the structures were vortexed. To remove any trace of detergents, the monolayers were transferred to ultrapure water and sonicated during 45 min on ice. The ultrapure water was removed by centrifugation at 5,000 rpm at 4°C for 5 min, the supernatant was discarded and the monolayers vortexed. Condensed cell monolayers were subjected to the action of 0.006% of DNase (Thermo Scientific, USA) with 10% AB for 96 h at 4°C and under 200 rpm. Lastly, the DNase solution was removed by centrifugation at 5000 rpm at 4°C for 5 min and

the supernatant was discarded (Figure 2.2). The resulted decellularized cell-derived matrix (dCDM) was then frozen and lyophilized for 48 h.
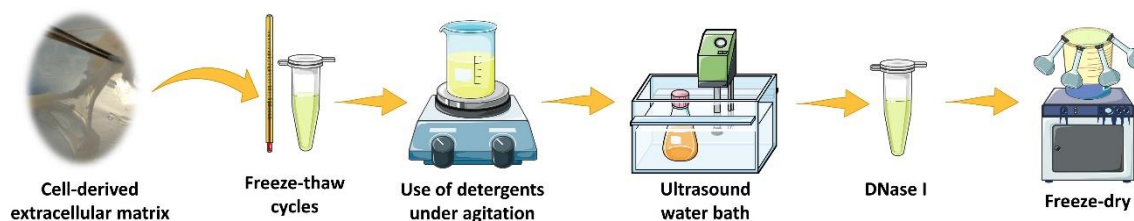

Figure 2.2 – Schematic representation of decellularization of cell-derived matrix process. Cell-derived matrices were subjected to the action of freeze-thaw cycles, detergents, sonication, DNase and finally freeze-drying.

2.1.1.4. Evaluation of decellularization effectiveness

The decellularization effectiveness was assessed through visualization of cell nuclei and matrix preservation by histology analysis, and DNA quantification. Herein, the decellularized tissue was transferred to histological cassettes and fixed with 10% (v/v) formalin solution. After paraffin embedding, samples were sectioned with 10 µm thickness by a microtome (Spencer 820, American Optical Company, USA). Standard hematoxylin and eosin (H&E; Thermo Scientific, USA) staining was performed to assess the presence of cell nuclei and Masson's trichrome (Bio-Optica staining kit, Italy) was performed to evaluate the preservation of collagen content. DNA extraction was performed by means of using the DNeasy Blood & Tissue Kit (Qiagen, Germany) and according to manufacturer's instructions. For DNA quantification Quant-IT PicoGreen dsDNA Assay Kit 2000 assays (Thermo Scientific, USA) was used according to the manufacturer's instructions. The fluorescence intensity was read at 485/20 nm (excitation) and 530/20 nm (emission) using a microplate reader (Synergy HT, Bio-Tek, USA) and the readings were converted into ng/ml using a standard curve that was produced with standard dsDNA solutions at different concentrations, ranging from 2,000 ng/ml to 250 ng/ml. Finally, the dsDNA quantification values were normalized by the dCDM dry weight.

2.1.1.5. dCDM solution preparation

The dCDM was dissolved using 1 ml of 0.01 M hydrochloric acid (Honeywell, USA) and 10 mg pepsin (Fisher Scientific, USA) per mg of CDM. The dCDM was placed in the solution under agitation at 200 rpm at room temperature for 72 h until it was fully dissolved. After this, the pH level was adjusted to 7.0.

2.1.1.6. Scaffold fabrication

For scaffold fabrication four different conditions were prepared, SF scaffolds (SF scaffolds), SF combined with multi-walled carbon nanotubes scaffolds (SF/CNT scaffolds), SF combined with dCDM scaffolds (SF/dCDM scaffolds) and SF combined with dCDM and CNT (SF/dCDM/CNT scaffolds). For SF scaffolds, SF solution was diluted to 8 wt% in distilled water and combined with horseradish peroxidase (HRP) (type VI, 0.84 mg/ml) (Sigma Aldrich, USA) and hydrogen peroxide solution (H_2O_2, 0.36 wt%; Panreac, Spain) this mixture was then incubated at 37°C for 30 min. To obtain SF/CDM scaffolds, SF solution was combined with dCDM solution for a final concentration of 8 wt% SF and 1 mg/ml of dCDM. For the SF/CNT scaffolds, SF was combined with CNT to an end concentration of 8 wt% SF and 1 mg/ml of CNT. The SF/CDM/CNT were fabricated combining SF, dCDM and CNT to an end concentration of 8 wt% of SF, 1 mg/ml of dCDM and 1 mg/ml of CNT. All scaffolds, SF/dCDM, SF/CNT, and SF/dCDM/CNT were fabricated as described for the development of SF scaffolds. In this reasoning, each solution was combined with HRP (type VI, 0.84 mg/ml) and hydrogen peroxide solution. This mixture was then incubated at 37°C for 30 min. After the enzymatic cross-linking the scaffolds were frozen at - 80°C for 2 h and then freeze-dried for 24 h (Figure 2.3).
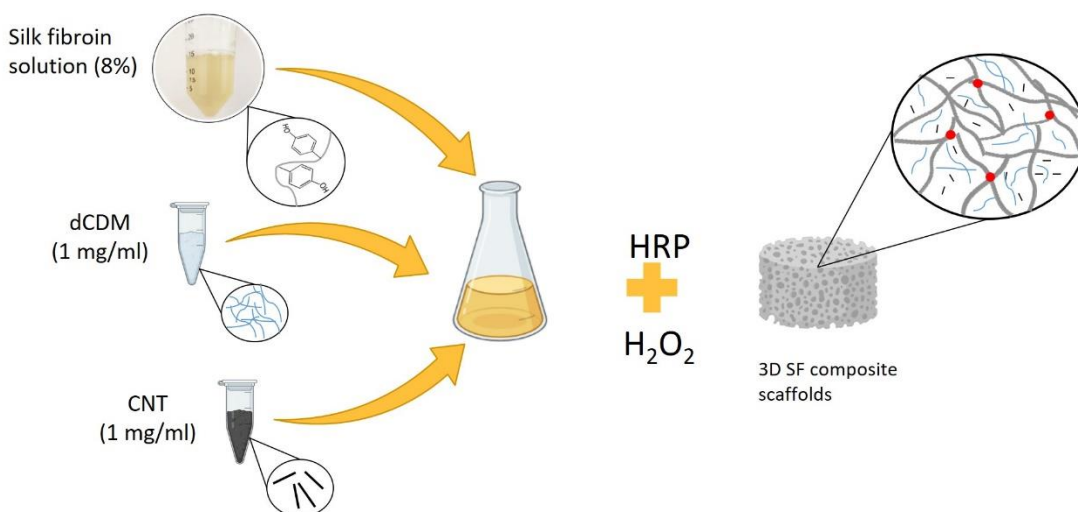
Figure 2.3 – Schematic representation of scaffold production. Overview of the scaffold fabrication procedure using enzymatic cross linking and freeze drying.

2.1.1.7. Micro computed tomography (Micro CT)

Micro-computed tomography is a 3D, high-resolution X-ray imaging technique. Micro-CT measures the decline of X-rays passing through tissues. The X-rays decline at different rates depending on the density of the tissues (2). The resulting images are obtained by stacking individual images in order to produce a three-dimensional view of the sample. This technique allows for the animation and quantification of regions of interest provided that density differences can be made by thresholding. This technique is cost-effective and can be used to examine the architecture of bone (2,3).

The micro-architecture of the produced scaffolds was investigated using a high-resolution micro-CT SkyScan 1272 scanner (Bruker, USA) with a pixel size of 10 μm. Standardized cone-beam reconstruction software (NRecon v1.4.3, SkyScan) was used for data sets reconstructions. Representative data set of the samples was segmented into binary images with a dynamic threshold of 22–40 (gray values). Then, the binary images obtained were used for morphometric analysis (CT Analyser, v1.5.1.5, SkyScan) and construction of 3D models (CTVox, v2.4, SkyScan).

2.1.1.8. Dynamic mechanical analysis (DMA)

DMA is technique used to study the viscoelastic properties of polymers. Using DMA it is possible to calculate the stiffness (modulus) of the material under stress through the magnitude of the applied stress and the consequent strain. More specifically, DMA works by measuring the stiffness and damping properties of materials by applying a sinusoidal load to a specimen and measuring the resultant deformation at different temperatures or frequencies (4,5).

The viscoelastic measurements were investigated using a DMA 8000 (PerkinElmer, USA) in the compressive mode. The scaffolds were immersed in PBS overnight at 37°C. The geometry of the scaffolds

was measured (with a micrometer of precision), clamped in the DMA apparatus and immersed in a PBS bath with the temperature set to 37°C. After equilibration at 37°C, the DMA spectra were obtained during a frequency scan between 0.1 and 10 Hz. A constant strain amplitude of 50 μm was applied in each experiment.

2.1.1.9. Bioactivity test

For a material to bond to living bone the formation of bone-like apatite on its surface when implanted in the body is necessary, this can be reproduced in simulated body fluid (SBF) with ion concentrations closely resembling those of the human plasma (6). This way, it is possible to predict *in vitro* bioactivity of a biomaterial by determining the ability of apatite formation on the material's surface in SBF (7).

The *in vitro* bioactivity evaluation was performed as described elsewhere (8). Briefly, scaffolds were soaked for 7 and 14 days into polystyrene flasks containing SBF. The SBF solution was prepared under continuous agitation of 60 rpm and at 37°C with ion concentrations similar to human blood as described in Table 2.1 (8). Then the pH was corrected to 7.4, which is nearly equivalent to those of human blood plasma. After, the scaffolds were washed with distilled water and allowed to dry at 37°C for 1 day and analyzed by means of SEM (JEOL, JSM-6010LV) and elemental chemical analysis by energy dispersive X-ray spectroscopy (EDS). All experiments were carried out in triplicate for each composition.

Table 2.1 – Concentration of ions composing the SBF solution.

Ion	Ion concentration (mM)
Na^+	142.0
K^+	5.0
Ca^{2+}	2.5
Mg^{2+}	1.5
Cl^-	148.8
HPO_4^-	1.0
HCO_3^{2-}	4.2
SO_4^{2-}	0.5

2.1.2. Cellular *in vitro* studies

2.1.2.1. Cell viability and morphology

The cell morphology was assessed by F-actin staining. First, cells were rinsed with PBS, fixed with 10% Neutral Buffered Formalin (ThermoFisher Scientific) for 20 min and permeabilized for 5 min with 0.1% v/v Triton X-100 (Sigma-Aldrich) in PBS. Afterwards, F-actin filaments were stained with Phalloidin–Tetramethylrhodamine B isothiocyanate (Sigma-Aldrich, 1:100) and nuclei were counterstained with 1:1000 of the stock of 4,6-Diamidino-2-phenyindole, dilactate solution (DAPI, 1mg/mL, Biotium). Samples were analysed by confocal microscopy (Leica TCS SP8).

Calcein AM is a cell-permeant dye used to detect living cells. In living cells, calcein AM is converted to calcein, which presents green-fluorescence making it detectable under a fluorescence microscope. On the other hand, propidium iodide (PI) is commonly used to detect dead cells since it is not a permanent dye and thus can only stain cells whose membrane has been disrupted. Calcein AM and PI are widely used in live/dead assays (9).The cell viability was assessed by calcein-AM and propidium iodide (Life Technologies, Carlsbad, USA) staining. At each time point, seeded scaffolds were incubated in 1 µg/ml calcein-AM and 5

µg/ml PI prepared in cultured medium for 30 min in the dark at 37°C in 5% CO_2. After, samples were immediately analyzed by confocal microscopy (Leica TCS SP8).

2.1.2.2. Cell seeding

All scaffolds were sterilized with oxide ethylene prior to cell seeding. Previously isolated hASCs were cultured at a density of 3,000 cells per cm^2 into a 150 cm^2 T-flask in α-MEM medium supplemented with 10% FBS and 1% AB and maintained at 37°C under a humidified atmosphere of 5% v/v CO_2 in air. The medium was changed twice a week until cells reached 80% of confluence. At this point cells were detached and seeded at the scaffolds. For that, a drop (30 µl) of 150,000 hASCs in medium was seeded on top of SF, SF/dCDM, SF/CNT, and SF/dCDM/CNT scaffolds. After 1 h at 37°C the drop was completely absorbed by the scaffolds and 1 ml of α-MEM medium with 10% FBS and 1% AB was added to each well. Cultures were maintained in 48 well non-adherent plates to avoid cell adhesion to the bottom of the plates. Cultures were maintained at 37°C under a humidified atmosphere of 5% (v/v) CO_2 in air.

2.1.2.3. Cell Viability

Alamar Blue is a resazurin-based solution that uses the reducing power of living cells to measure their metabolic activity (10). The reduction of resazurin into resorufin is caused by chemical reduction reactions of the cells respiratory chain. Resorufin possesses fluorescence and thus its concentration can be determined fluorescence spectroscopy (excitation between 530–560 nm and an emission at 590 nm). Differences in resorufin detection can be associated with differences in metabolic activity of cell and infer on the cells viability (11).

Cell viability was assessed after 1, 14 and 21 days using 20% (v/v) of Alamar Blue reagent (ALAMAR BLUE®, AbD, UK) in α-MEM culture medium, followed by 3 h of incubation at 37°C with 5% CO_2 and protected from light. Afterwards, 100 µL of supernatant was transferred from each well in triplicate to a new 96-well cell culture plate. Fluorescence intensity was read at 530/20 nm (excitation) and 590/35 nm (emission) using a microplate reader (Synergy HT, Bio-Tek, USA). Alamar Blue in medium was used as a blank. Values were normalized with DNA values for each time point.

2.1.2.4. DNA Content

DNA content was assessed after 1, 14 and 21 days of culture. Scaffolds were washed with PBS and 1 ml of ultra-pure water was added into each well and incubated at 37°C for 1 h. Scaffolds were then stored at −20°C until analysis. Before DNA quantification, the samples were placed in an ultrasound bath for 30 min at 37°C to ensure for cell lysis. Quant-IT PicoGreen dsDNA Assay Kit 2000 assays was used according to the manufacturer's instructions to quantify dsDNA from cell lysates. The fluorescence intensity was read at 485/20 nm (excitation) and 530/20 nm (emission) using a microplate reader and the readings were converted while using a standard curve that was produced with standard dsDNA solutions at different concentrations.

2.1.2.5. Histology staining

Hematoxylin and eosin staining is the most frequently used dye in histology for assessing formalin-fixed, paraffin-embedded tissue sections (12). The negatively charged affinity of acidic eosin for cytoplasmic proteins, and the positively charged affinity of basic hematoxylin for nuclear structures make it ideal for histological applications (13).

Samples were collected after 1, 14 and 21 days and processed for histology. In this sense, constructs were transferred to histological cassettes and fixed with 10% (v/v) formalin solution. After paraffin embedding (Microm EC350-1, Thermo Scientific, USA), samples were processed in a spin tissue processer (Microm STP 120, Thermo Scientific, USA) and sectioned with 10 μm thickness by a microtome (Spencer 820, American Optical Company, USA). Standard hematoxylin and eosin (H&E; Thermo Scientific, USA) staining was performed using an automatic stainer (Microm HMS 7740, Thermo Scientific, USA) to assess cell distribution and collagen deposition by Masson's trichrome (Bio-Optica staining kit, Italy).

2.1.2.6. Scanning Electron Microscopy

Scanning electron microscopy (SEM, JSM-6010 LV, JEOL, Japan) was used to assess the microstructure of the scaffolds and observe the cell morphology after the seeding. For SEM analysis, the samples were cut into cross-sections, and the internal surface of the scaffolds was observed. Scaffolds were fixated in formalin 10% and prior to analysis sputter-coated with gold using a Leica EM ACE600 coater (Leica Microsystems, Austria). For the cell-seeded scaffolds, these were fixated in formalin 10% and rehydrated with a series of ethanol concentrations (30, 50, 70, 90 and 10% v/v), twice each concentration for 15 min, lastly the scaffolds were placed in hexamethyldisilazane and left overnight at room temperature (RT) to dry. Prior to analysis the scaffolds were sputter-coated with gold using a Leica EM ACE600 coater (Leica Microsystems, Austria).

2.1.2.7. Alkaline phosphatase activity quantification

ALP is a membrane-bound metalloenzyme that plays an important role in bone mineralization (14). Thus, the ALP activity has been widely used as an early marker for *in vitro* osteoblastic phenotype characterization (15).

To quantify ALP activity, cell lysate previously produced was used. For that, 80 µl of cell lysate were combined with 20 µl of 1.5 M of Alkaline buffer solution (Sigma-Aldrich) and 100 µl of 4 mg/ml of phosphatase substrate (Sigma-Aldrich, USA). Then samples were incubated in the dark for 1 h at 37 °C. At this point, the reaction was stopped by adding 100 µl of 0.3 M of NaOH (PanReac AppliChem) and the absorbance was read at 405 nm using a microplate reader. The ALP activity per h was determined using a standard curve obtained from different dilutions of 4-Nitrophenol (Sigma-Aldrich) solution 10 mM, ranging from 0 to 250 µM and normalized by the dsDNA quantification values.

2.1.2.8. RNA Isolation and Real-Time Quantitative Reverse Transcriptase-Polymerase Chain Reaction (qRT-PCR)

Real-time quantitative reverse transcriptase PCR is a valuable tool for analyzing RNA. A reverse transcriptase approach is comprised by a few basic steps, in which the first step is the extraction, isolation and quantification of the samples RNA. Afterwards the enzyme reverse transcriptase is used to obtain a complementary single-strand DNA copy. This step requires the use of oligonucleotide primers, which can be specific and non-specific, to anneal with the RNA in order to obtain a cDNA strand. Following the reverse transcriptase reaction, the cDNA strand is amplified by PCR (16).

The total mRNA from the seeded scaffolds was extracted using the Direct-zolTM RNA MiniPrep kit (Zymo Research, USA), following the manufacturer's instructions. Briefly, after 1, 14 and 21 days of culture, the constructs were washed with PBS solution, immersed in 300 µl of TRI Reagent, and storage at −80°C until further use. Samples were thawed at room temperature and sonicated using an ultrasonic processor (Sonics Materials VCX-130PB Ultrasonic Processor, USA) to completely lyse the cells. The total RNA pellets were reconstructed in RNase-free water (Gibco, Life Technologies, USA). For RNA quantification determination, a NanoDrop ND-1000 spectrophotometer (Nano-Drop Technologies, USA) was used. Complementary DNA (cDNA) synthesis was performed according to the protocol from the qScriptTM cDNA synthesis Kit (Quanta Biosciences, USA) using a MiniOpticon real-time PCR detection system (BioRad, USA), where 100 ng of total RNA was used to obtain single-stranded cDNA with qScript Reverse Transcriptase (RT). The cDNA was further used as a template for the amplification of osteogenic (ALP, Runx-2, Col Iα and OPN) genes (Table 2.2) using the PerfeCta SYBR Green FastMix kit (Quanta Biosciences, USA) according to the manufacturer's instructions. Forty-five cycles of denaturation (95°C, 10 s), annealing (temperature specific for each gene, 25 s), and extension (72°C, 30 s) were carried out in a Mastercycler ep realplex real-time PCR system (Eppendorf, Germany). The transcript expression data of each sample were normalized to the housekeeping gene glyceraldehyde-3-phosphate-dehygrogenase (GAPDH) of that sample, for each tested time point. The relative gene expression was calculated according to the Livak ($2-\Delta\Delta$Ct) method, considering the day 1 condition as the calibrator.

Table 2.2- List of primer sequences used to amplify osteogenic-related markers.

Gene	Sequences		T_m (°C)
	Forward (5'–3')	Reverse (5'–3')	
GAPDH	ACAGTCAGCCGCATCTTCTT	GACAAGCTTCCCGTTCTCAG	58.4
Col Iα	CGAAGACATCCCACCAATCAC	GTCACAGATCACGTCATCCGC	59.6
ALP	CTCCTCGGAAGACACTCTG	AGACTGCGCCTGGTAGTTG	60
OPN	CCCACAGACCCTTCCAAGTA	GGGGACAACTGGAGTGAAAA	58.4
Runx-2	TTCAGACCAGCAGCACTC	CAGCGTCAACACCATCATTC	58.1

2.1.2.9. Hemolytic assay

Adverse interactions between biomaterials and blood should be thoroughly analyzed to prevent destruction of blood components. One of the major criteria which limit clinical applicability of blood-contacting biomaterials is hemocompatibility (17).

To assess the hemolytic activity levels of developed scaffolds, 5 ml of blood were mixed with 45 ml of PBS. Then, to obtain the red blood cells, samples were centrifuge (1,000× g, 4°C) during 10 min and the supernatant was discarded. The centrifugation step was repeated until obtain clear OBS solution, thus indicating that the pellet was clean. Afterwards, the obtained pellet was measured and combined with PBS to make a solution of 3% (w/V). At this point, 80 μl of this solution was transferred into a well of a 96-well plate and each developed scaffold was placed inside the solution. As positive control (*i.e.* 100% red blood cell lysis), 80 μl of Triton X-100 was added to the solution, while as negative control (i.e. 0% red blood cell lysis), 80 μl of PBS was added. The plates were incubated at 37°C during 4 h, and afterwards centrifuged at 1000× g for 10 min, at 4°C. Finally, the supernatant (80 μl) of each well was transferred into a new 96-well plate and the absorbance was measured at 558 nm. For each sample 3 wells were prepared and data was normalized with the controls, using the following formula:

Hemolysis (%) = [(Abs sample/Abs Triton X-100) − 1] × 100   (Equation 2.1)

2.1.3.Statistical analysis

Statistical analyses were performed using GraphPad Prism 6.07. First, Shapiro-Wilk test was performed to assess data normality. Non-parametric Mann-Whitney test was used to determine the differences for the qRT-PCR results, whereas the non-parametric Kruskal-Wallis test followed by Dunn's test for multiple comparisons, were used for the analysis of the ALP expression results, metabolic activity, and cell proliferation. The critical level of statistical significance was $p < 0.05$. Data are presented as mean ± standard deviation.

2.1.4. References

1.   Maia FR, Reis RL, Oliveira JM. Decellularized hASCs-derived matrices as biomaterials for 3D in vitro approaches. Methods in cell biology. 2020;156:45–58.

2.   van der Horst G, Buijs JT, van der Pluijm G. Chapter 46 - Pre-clinical molecular imaging of "the seed and the soil" in bone metastasis. In: Heymann DBT-BC (Second E, editor. San Diego: Academic Press; 2015. p. 557–70.

3.   Assad M, Jackson N. Biocompatibility Evaluation of Orthopedic Biomaterials and Medical Devices: A Review of Safety and Efficacy Models. In: Narayan RBT-E of BE, editor. Oxford: Elsevier; 2019. p. 281–309.

4.   Bergström J. 2 - Experimental Characterization Techniques. In: Bergström JBT-M of SP, editor. William Andrew Publishing; 2015. p. 19–114.

5.   Broughton W. 6 - Testing the mechanical, thermal and chemical properties of adhesives for marine environments. In: Weitzenböck JRBT-A in ME, editor. Woodhead Publishing Series in Welding and Other Joining Technologies. Woodhead Publishing; 2012. p. 99–154.

6.   Kokubo T. Bioactive glass ceramics: properties and applications. Biomaterials. 1991;12(2):155–63.

7.   Erceg I, Selmani A, Gajović A, Radatović B, Šegota S, Ćurlin M, et al. Precipitation at Room Temperature as a Fast and Versatile Method for Calcium Phosphate/TiO(2) Nanocomposites Synthesis. Nanomaterials (Basel, Switzerland). 2021 Jun 9;11(6):1523.

8.   Cüneyt Tas A. Synthesis of biomimetic Ca-hydroxyapatite powders at 37°C in synthetic body fluids. Biomaterials. 2000;21(14):1429–38.

9.   Freeberg MAT, Kallenbach JG, Awad HA. Assessment of Cellular Responses of Tissue Constructs in vitro in Regenerative Engineering. In: Narayan RBT-E of BE, editor. Oxford: Elsevier; 2019. p. 414–26.

10.   Bonnier F, Keating ME, Wróbel TP, Majzner K, Baranska M, Garcia-Munoz A, et al. Cell viability assessment using the Alamar blue assay: A comparison of 2D and 3D cell culture models. Toxicology in Vitro. 2015;29(1):124–31.

11.   O'Brien J, Wilson I, Orton T, Pognan F. Investigation of the Alamar Blue (resazurin) fluorescent dye for the assessment of mammalian cell cytotoxicity. European journal of biochemistry. 2000 Sep;267(17):5421–6.

12.   Sarnat HB, Carpenter S. Chapter 4 - Muscle Biopsy for Diagnosis of Neuromuscular and Metabolic Diseases. In: Darras BT, Jones HR, Ryan MM, De Vivo Childhood, and Adolescence (Second Edition) DCBT-ND of I, editors. San Diego: Academic Press; 2015. p. 46–65.

13.   Maxie MG, Miller MA. Chapter 1 - Introduction to the Diagnostic Process. In: Maxie Kennedy & Palmer's Pathology of Domestic Animals: Volume 1 (Sixth Edition) MGBT-J, editor. W.B. Saunders; 2016. p. 1-15.e1.

14.   Sharma U, Pal D, Prasad R. Alkaline phosphatase: an overview. Indian journal of clinical biochemistry : IJCB. 2013/11/26. 2014 Jul;29(3):269–78.

15.   Matta C, Szűcs-Somogyi C, Kon E, Robinson D, Neufeld T, Altschuler N, et al. Osteogenic differentiation of human bone marrow-derived mesenchymal stem cells is enhanced by an aragonite scaffold. Differentiation. 2019;107:24–34.

16.   Freeman WM, Walker SJ, Vrana KE. Quantitative RT-PCR: pitfalls and potential. BioTechniques. 1999 Jan;26(1):112-122,124-125.

17.   Weber M, Steinle H, Golombek S, Hann L, Schlensak C, Wendel HP, et al. Blood-Contacting Biomaterials: In Vitro Evaluation of the Hemocompatibility. Frontiers in bioengineering and biotechnology. 2018;6:99.

CHAPTER III.

Results and Discussion

CHAPTER III. Results and Discussion

3.1. Results

Various characterization and biological assays were performed to assess the viability and cytocompatibility of the developed scaffolds. hASCs were cultured on four different scaffolds formulations: SF, SF/dCDM, SF/CNT and SF/dCDM/CNT scaffolds, where SF scaffolds were used as control.

3.1.1. Scaffolds characterization

3.1.1.1. Evaluation of decellularization effectiveness

Hematoxylin and eosin and Masson's Trichrome staining were performed on the decellularized condensed monolayers to verify the presence of nuclei and collagen respectively, in order to confirm successful decellularization. As it can be observed from Figure 3.1, nuclei were successfully removed from dCDM, while collagen was maintained as compared with control (CTRL), *i.e.* no decellularized matrices. Furthermore, the efficiency of the decellularization process was confirmed through dsDNA quantification analysis. Results show that the value of DNA was inferior to 50 ng/mg of dCDM dry weight, the accepted threshold for effective decellularization (1).
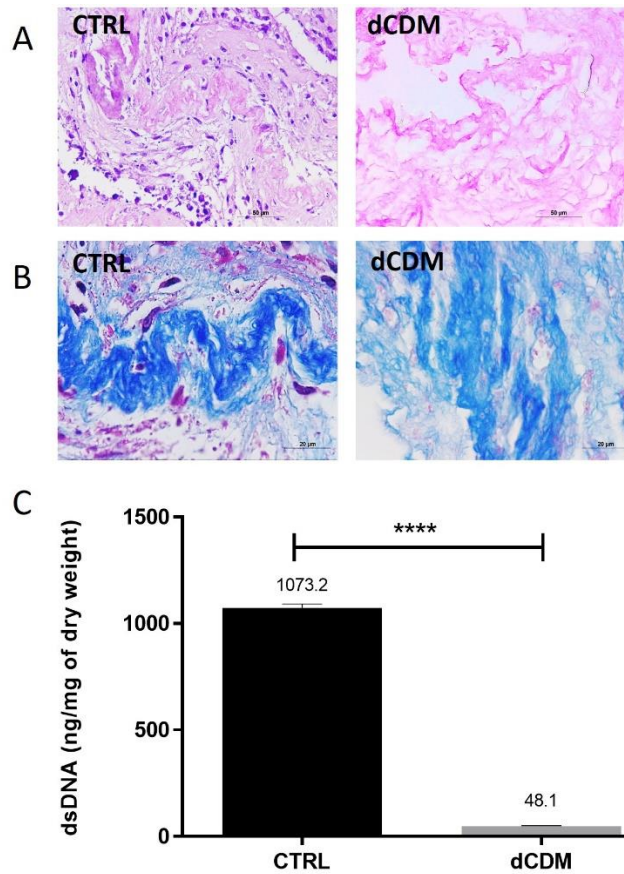
Figure 3.1 – Characterization of decellularized material. A) dCDM stained with hematoxylin and eosin showing no nucleus present. B) Masson's Trichrome staining performed on the CTRL and dCDM evidencing the collagen content (scale bar: 50 µm). C) dsDNA quantification showing a drastic reduction of dsDNA content on dCDM as compared with CTRL, reaching less than 50 ng/mg of dCDM dry weight as postulated (****$p \leq 0.0001$)

3.1.1.2. Scaffold's structure evaluation

Scaffolds composed by SF, SF/dCDM, SF/CNT and SF/dCDM/CNT were prepared and characterized using micro-CT, SEM and DMA. The micro-CT and SEM were performed to analyze the porosity and structure of the scaffolds (Figure 3.2). The micro-CT analysis showed differences in pore size (Figure 3.2 A). As seen in Table 3.2, SF evidenced a mean pore size of 83 ± 9 µm, SF/dCDM a pore size of 135 ± 34 µm, SF/CNT and SF/dCDM/CNT a pore size of 63 ± 29 µm and 112 ± 22 µm, respectively. Additionally, the total porosity of SF was 73 ± 3%, of SF/dCDM was 76 ± 4% and SF/CNT and SF/dCDM/CNT displayed a total porosity of 60 ± 3% and 75 ± 3%, respectively. SF/dCDM and SF/dCDM/CNT presented the highest total porosity and highest mean pore size. The values for mean trabecular thickness were very similar for all conditions.

Table 3.2 – Micro-CT analysis results. Total porosity (%), mean pore size (μm) and mean trabecular thickness (μm) for SF, SF/dCDM, SF/CNT and SF/dCDM/CNT scaffolds.

	Total porosity (%)		Mean pore size (μm)		Mean trabecular thickness (μm)	
Samples	Mean	stdev	Mean	stdev	Mean	stdev
SF	73	3	83	9	37	5
SF/dCDM	76	4	135	34	35	5
SF/CNT	60	3	63	29	36	8
SF/dCDM/ CNT	75	3	112	22	39	6

Images of scaffolds structure obtained by micro-CT clearly shows the different pore size (Figure 3.2 A), corroborating the values obtained during quantitative analysis (Table 3.2). Nevertheless, it is important to point out that no effect was observed in the size of the scaffolds, being all with ≈ 6 mm of diameter (Figure 3.2 A insets). Moreover, different densities of the different constituents of the scaffolds was observed, as depicted in Figure 3.2 B. In this sense, it is possible to detect the presence of dCDM (in blue) since it presents higher density than SF (in green), as well as the presence of CNT (in blue), being the formulation with dCDM and CNT the one with more differences in the density of the scaffold (Figure 3.2 B). Finally, SEM analysis clearly evidenced the different porosities of the scaffolds in accordance of the results obtained by micro-CT (Figure 3.2 C).
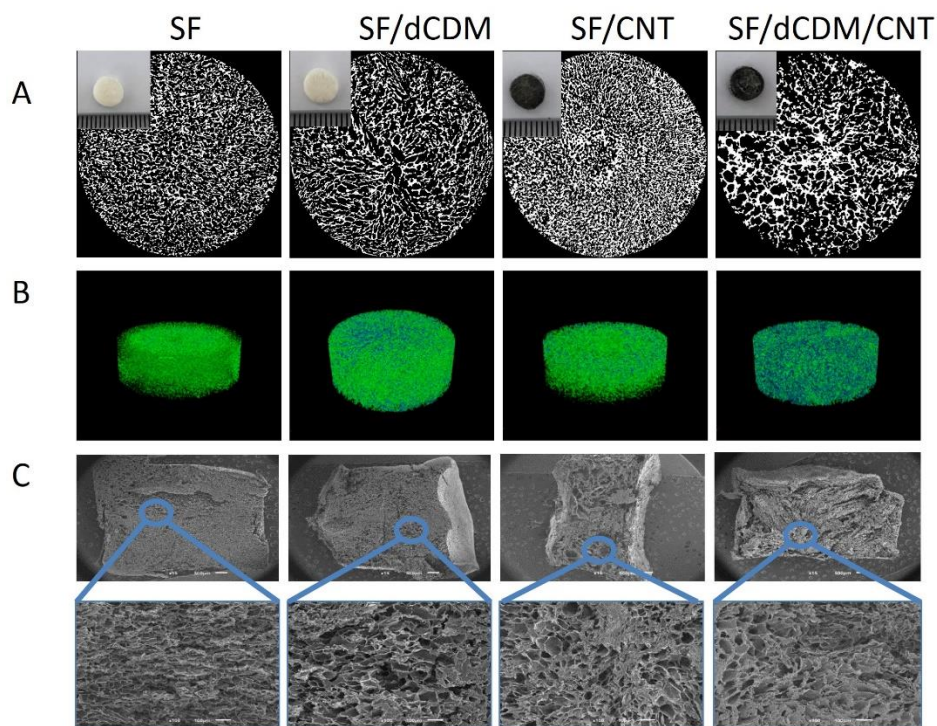
Figure 3.2 – Micro-CT and SEM analysis of SF, SF/dCDM, SF/CNT and SF/dCDM/CNT scaffolds. (A) Micro-CT images showing scaffolds porosity. The inset shows pictures of the different scaffolds. (B) Visibility of different densities of the materials that constitute the scaffolds. (C) SEM images showing the topography of scaffolds (scale bar: 500 µm) and in higher magnification the respective porosity (scale bar: 100 µm).

Furthermore, using micro-CT analysis it was possible to assess the dispersion and possible aggregation of the CNT (Figure 3.3). Using SF/dCDM as baseline and taking into consideration that the used threshold does not possesses the sensibility to detect individual nanotubes due to the technique's limitations (applied threshold between 25-255 (total content) and 75/85-255 for differentiation of CNT) it was possible to see that overall the formation of carbon nanotubes aggregates was low indicating an adequate homogeneity in the scaffold matrix.
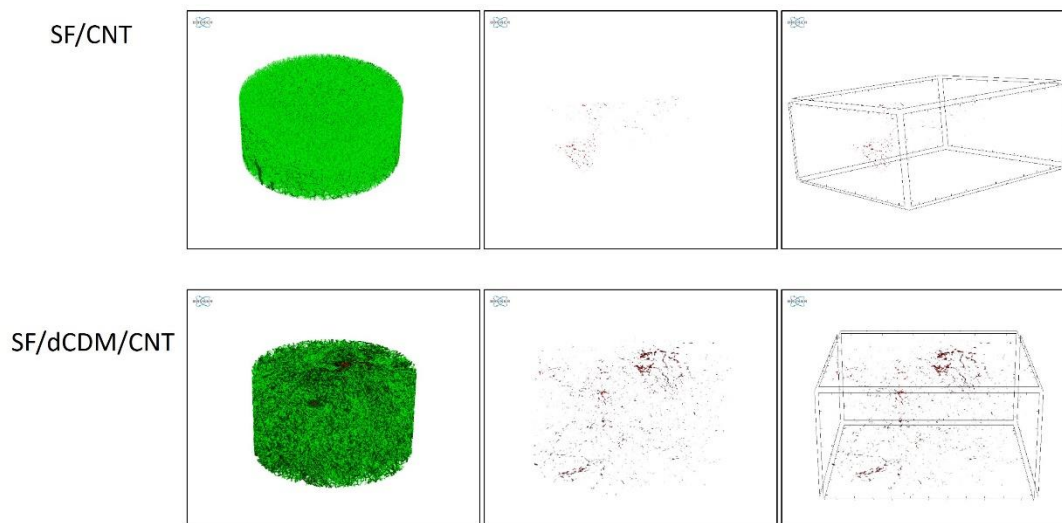
Figure 3.3 – Evaluation of carbon nanotube dispersion. Micro-CT analysis of SF/CNT and SF/dCDM/CNT showing nanotube aggregates (red regions) based on density, with SF/dCDM serving as baseline.

Concerning DMA, it was performed to assess the mechanical properties of the scaffolds, showing that conditions containing dCDM (SF/dCDM and SF/dCDM/CNT scaffolds) possess approximately ten times lower E' (kPa) values as compared with SF and SF/CNT scaffolds (Figure 3.4 A). Tan δ was also analyzed showing values below 1.0 that were constant up to 4 Hz for all conditions, evidencing that scaffolds' mechanical properties can be situated in the leathery region, meaning the scaffolds are tough but flexible (Figure 3.4 B).
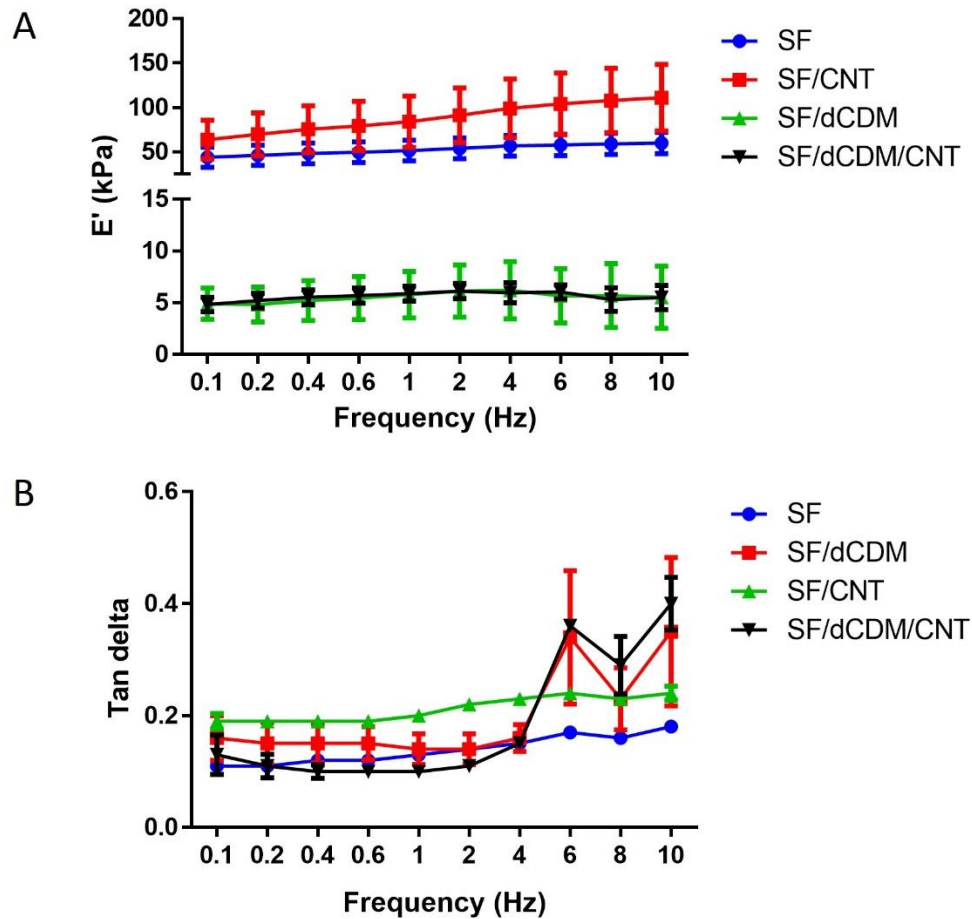
Figure 3.4 – DMA analysis. (A) Storage modulus (E'), and (B) Tan delta (Tanδ) of SF, SF/dCDM, SF/CNT and SF/dCDM/CNT scaffolds measured as function of frequency. Data is presented as mean ± stdev (n=3).

3.1.1.3. *In vitro* bioactivity assessment

Bioactivity was investigated by means of soaking SF, SF/dCDM, SF/CNT and SF/dCDM/CNT scaffolds in SBF at 37°C for 14 days. In order to evaluate mineralization formation, EDS was performed and SEM images were obtained. For all conditions, mineralization was verified after 14 days as depicted in Figure 3.5. Additionally, the formation of apatite crystals "cauliflower-like" structures on all conditions with exception of SF/CNT was verified. The SF/dCDM/CNT scaffolds showed higher amounts of calcium (Ca) and phosphate (P) as compared with SF/dCDM and SF/CNT scaffolds. When comparing SF scaffolds and SF/dCDM/CNT scaffolds, despite the similar values concerning the Ca content, it was observed lower values on P in SF/dCDM/CNT scaffolds.
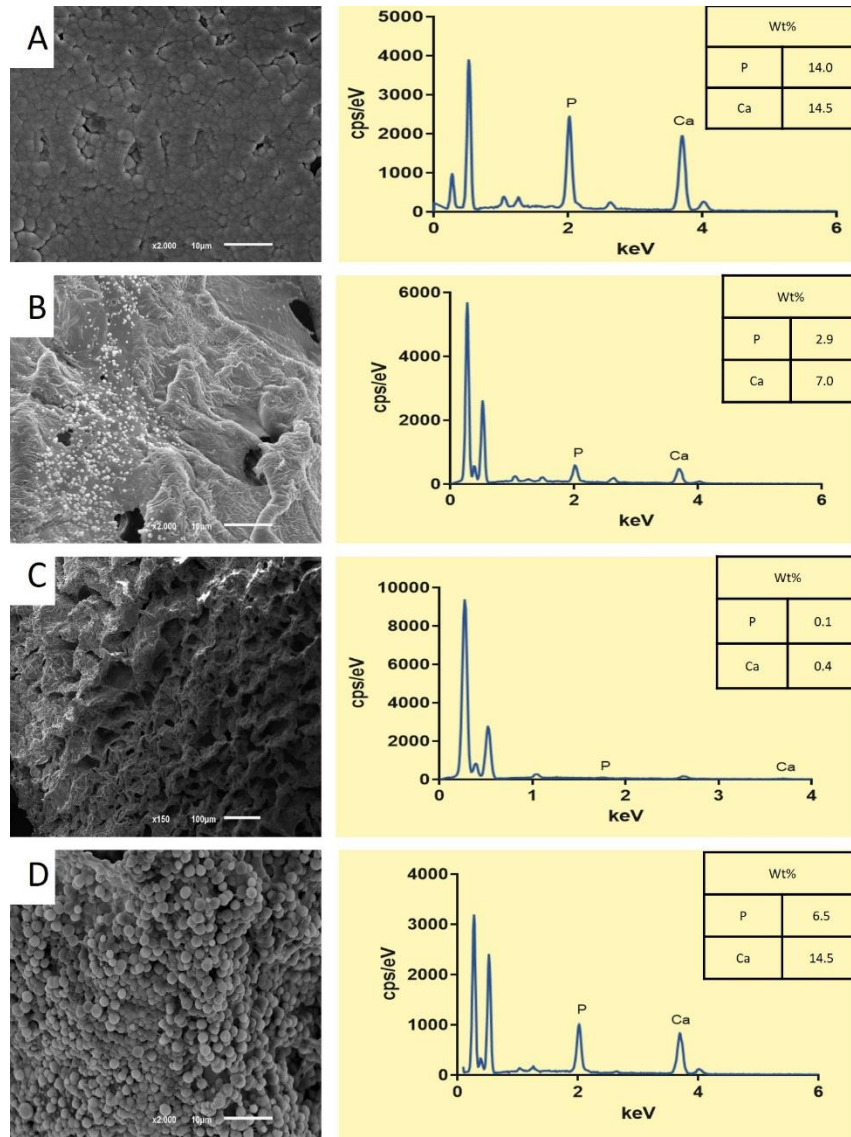
Figure 3.5 - In vitro bioactivity of SF, SF/dCDM, SF/CNT and SF/dCDM/CNT scaffolds. Representative SEM images and EDS analysis at day 14 of: (A) SF; (B) SF/dCDM; (C) SF/CNT; and (D) SF/dCDM/CNT (scale bar: 10 μm).

3.1.2. Cellular *in vitro* studies

3.1.2.1. Cell viability and morphology

After 1, 14 and 21 days cell viability and morphology were evaluated (Figure 3.12). Live/dead was performed to assess cell viability, staining live cells in green and dead cells in red. For all conditions cells remained viable along the time of culture as depicted in Figure 3.12. After 21 days, a high number of viable

cells was seen contrasting with the low number of dead cells. Additionally, it was possible to observe that cells proliferated along the 21 days. To assess the morphology of cells, the cytoskeleton was stained using Phalloidin (in red), and nucleus was stained with DAPI (blue colour). As it can be observed from Figure 3.12 insets, cells presented a round shape after 1 day of culture, but they shift to a spindle-like shape along the culture for all conditions.
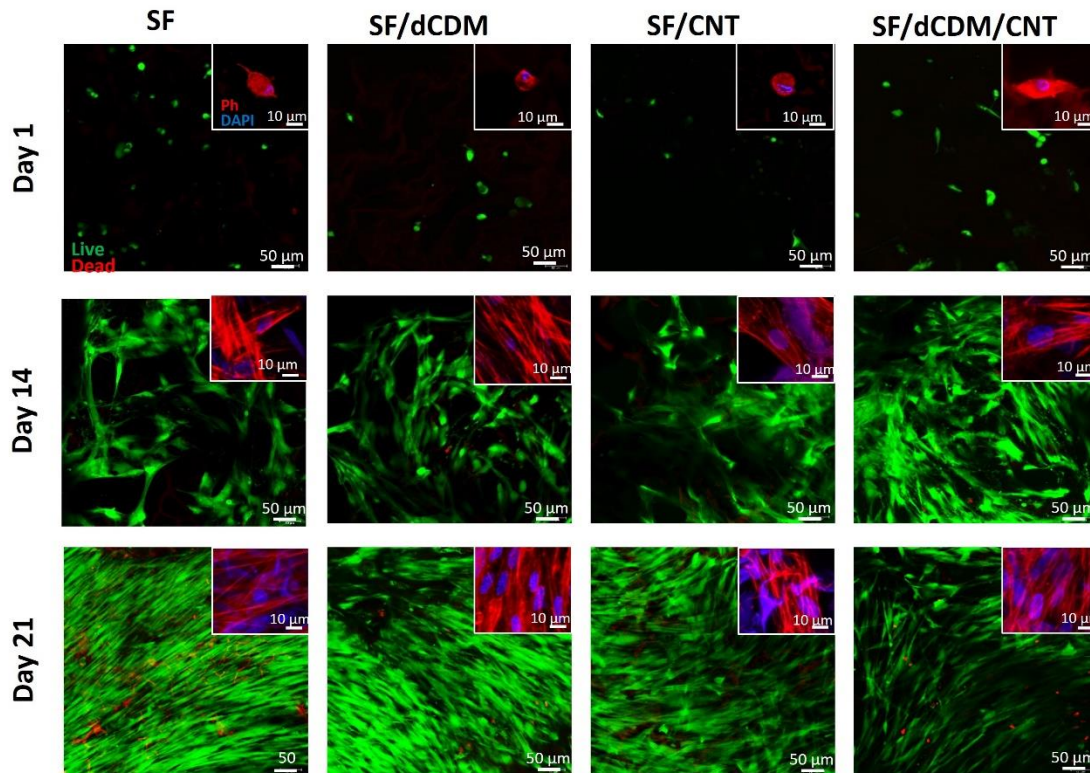

Figure 3.12 – Cell viability and morphology. Representative images of viability and morphology of hASCs cultured on SF scaffolds, SF/, SF/CNT scaffolds and SF/dCDM/CNT scaffolds through 21 days. Live/dead imaging showing viable cells stained in green and dead cells stained in red (scale bar: 50 μm). The inset pictures show cells' cytoskeleton and nucleus upon stained with Phalloidin (in red) and DAPI (in blue), respectively (scale bar: 10 μm).

3.1.2.2. Metabolic activity

Metabolic activity was analyzed using Alamar Blue assay at 1, 14 and 21 days (Figure 3.6). The results were normalized using dsDNA quantification values. It was verified that the cells remained metabolic active after 21 days in each of the conditions. At day 1, cells cultured on SF/dCDM/CNT scaffolds showed highest metabolic activity among the four conditions, and the cells cultured on SF and SF/dCDM scaffolds

showed the lowest metabolic activity. At day 14, the metabolic activity of cells cultured on SF/dCDM, SF/CNT and SF/dCDM/CNT scaffolds decreased as compared to day 1, while increasing for SF scaffolds. Nevertheless, cells cultured onto the SF/dCDM/CNT scaffolds also displayed highest metabolic activity, and SF and SF/dCDM the lowest values. Finally, at day 21, it was observed that the metabolic activity of cells cultured onto the SF/dCDM/CNT scaffolds decreased, but an increase in cells cultured onto the SF scaffolds was observed. When comparing metabolic activity values of day 14 and day 21, it was possible to observe a significant increase of metabolic activity values for SF, SF/dCDM and SF/CNT cell-laden scaffolds. Moreover, the results showed that cells cultured onto SF/CNT scaffolds had significantly higher metabolic activity as compared to the other three types of scaffolds at day 21.
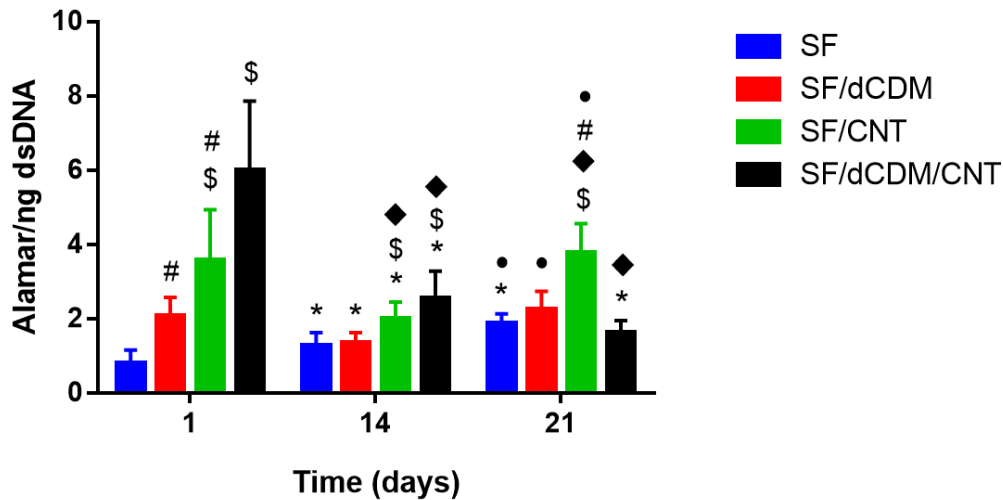

Figure 3.6 – Metabolic activity of cells seeded on scaffolds. Metabolic activity of hASCs seeded on SF, SF/dCDM, SF/CNT and SF/dCDM/CNT scaffolds evaluated using Alamar Blue assay and normalized by ng of dsDNA. * - denotes statistically significant differences when compared with day 1; $ - denotes statistically significant differences when compared with SF at the same time-point; # - denotes statistically significant differences when compared with SF/dCDM/CNT at the same time-point; ♦ - denotes statistically significant differences when compared with SF/dCDM at the same time-point. ● – denotes statistically significant differences between day 21 and day 14. Data is presented as mean±stdev (n=9).

3.1.2.3. Cell Proliferation

Cell proliferation was also analyzed as shown in Figure 3.7. For that, dsDNA was quantified at 1, 14 and 21 days of culture. At day 1, SF/dCDM scaffolds showed higher rates of cell proliferation than SF/CNT.

At day 14, comparatively to day 1, there was a significant increase in cell proliferation for all four conditions. Furthermore, SF/dCDM scaffolds displayed the highest amount of cell proliferation at this time point while the lowest increase was verified in the SF/CNT scaffolds condition. When analyzing the values of cell proliferation at day 21, it increased in significantly in all conditions comparatively to day 1. Interestingly, when comparing day 21 and day 14, SF/CNT samples displayed an increase of cell proliferation values. At day 21, it was verified that SF/dCDM/CNT samples presented higher cell proliferation than SF/dCDM and SF/CNT, but no differences were observed when compared with SF.
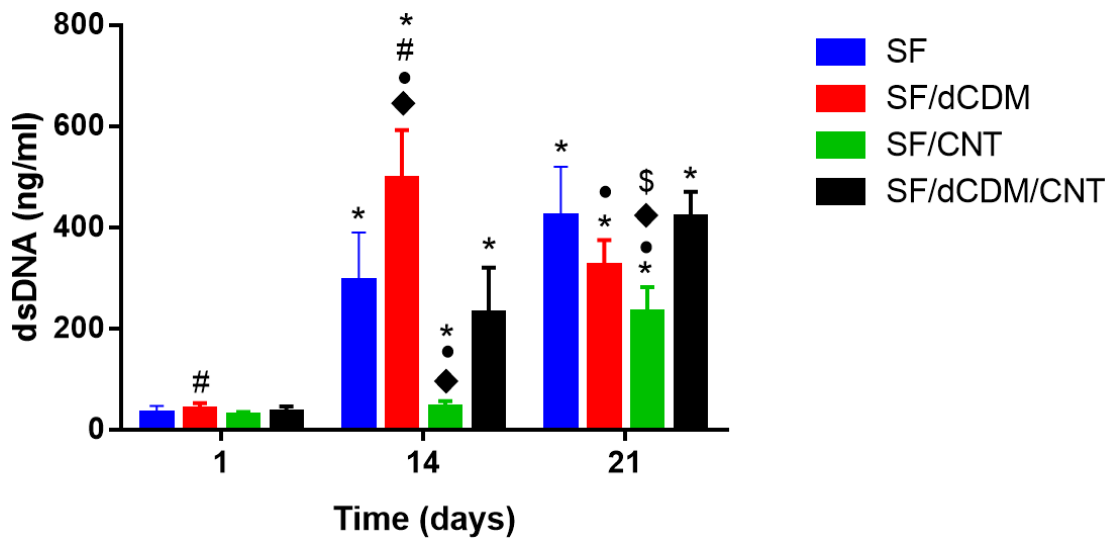
Figure 3.7 - DNA quantification of hASCs seeded on SF, SF/dCDM, SF/CNT and SF/dCDM/CNT. * - denotes statistically significant differences when compared with day 1; # - denotes statistically significant differences when compared with SF/CNT; ● - denotes statistically significant differences when compared to SF/dCDM/CNT; ♦ - denotes statistically significant differences when compared with SF. $ - denotes statistically significant differences when compared to day 14. Data is presented as mean±stdev (n=9).

3.1.2.4. Histology and SEM analysis

Histological analysis was performed on the seeded scaffolds after 21 days to assess the cell dispersion, morphology and collagen production. Masson's Trichrome (TM) was performed to assess the collagen content on cell seeded scaffolds. After 21 days, collagen was observed surrounding the cells for conditions SF, SF/dCDM and SF/dCDM/CNT, but no collagen was detected for SF/CNT conditions.

Hematoxylin and eosin (HE) staining was performed to observe cells grown on the scaffolds. The HE staining showed that after 21 days, cells were clearly visible on the scaffold for all 4 conditions with some level of penetration into the scaffolds (Figure 3.8, black arrows).
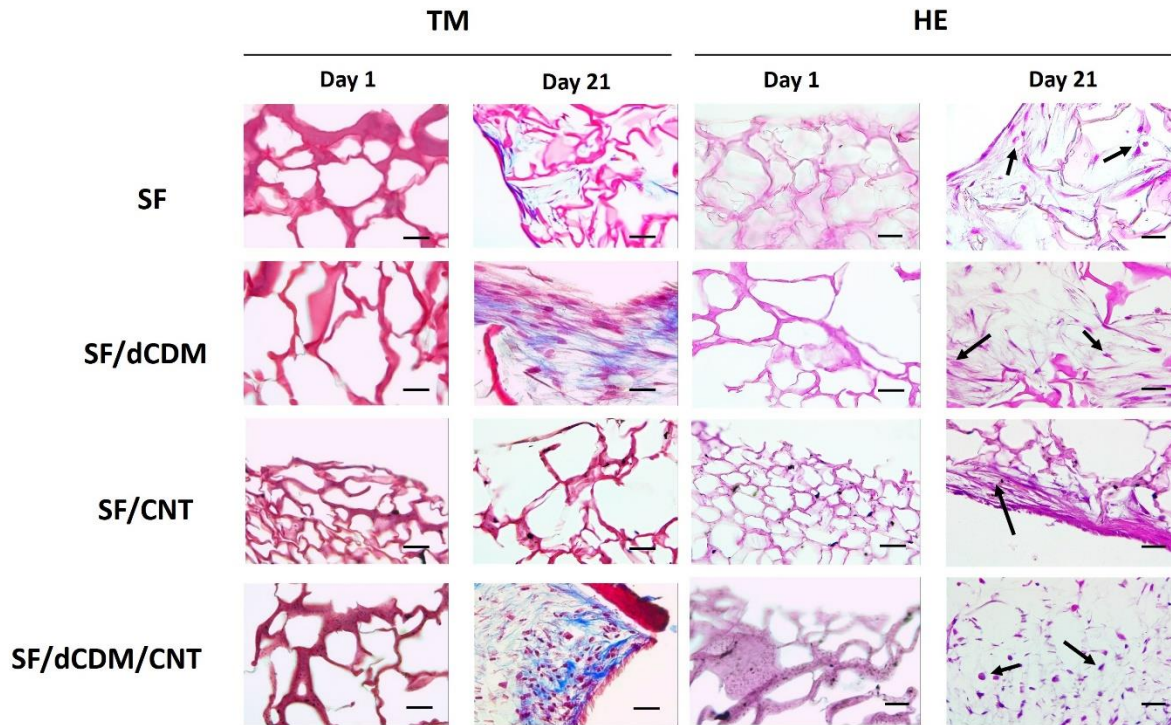
Figure 3.8 – Histological analysis. Representative images of Masson's Trichrome (TM) of hASCS cultured on SF, SF/dCDM, SF/CNT and SF/dCDM/CNT scaffolds at day 1 and 21, staining collagen in blue (scale bar: 50 μm). Representative images of hematoxylin and eosin (HE) staining of hASCS cultured on SF, SF/dCDM, SF/CNT and SF/dCDM/CNT scaffolds at day 1 and 21 (scale bar:50 μm; black arrows indicate stained cells).

To further complement this data, SEM was performed after 21 days. As expected scaffolds were completely covered in cells with a high degree of confluence (Figure 3.9).
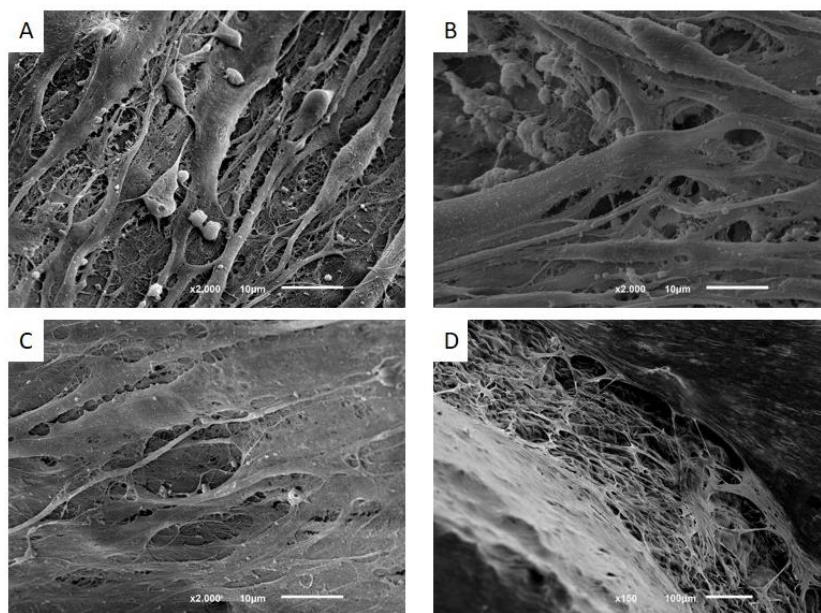
Figure 3.9 – SEM analysis. Visible cells covering (A) SF scaffolds, (B) SF/dCDM scaffolds, (C) SF/CNT scaffolds and (D) SF/dCDM/CNT scaffolds after 21 days of culture (scale bar: 10 µm).

3.1.2.5. ALP activity quantification

The quantification of ALP activity was performed after 1, 14 and 21 days of culture and normalized by the amount of dsDNA (Figure 3.10). At day 1, SF and SF/dCDM scaffolds had significantly lower ALP expression than SF/CNT and SF/dCDM/CNT conditions. At day 14, comparatively to day 1, the values of ALP activity decreased for SF/dCDM scaffolds, while the values increased for SF/CNT scaffolds. Furthermore, similarly to day 1, SF samples had significantly lower ALP expression than SF/CNT and SF/dCDM/CNT, whereas SF/dCDM showed lower expression than SF/dCDM and SF/dCDM/CNT samples. At day 21, comparatively to day 1, a decrease in expression was observed for SF, SF/dCDM and SF/dCDM/CNT scaffolds. Also, comparatively to day 14, a decrease in ALP expression for SF/CNT and SF/dCDM/ CNT scaffolds was verified. Following the tendency of the previous time points the expression of SF/CNT was higher than the other conditions.
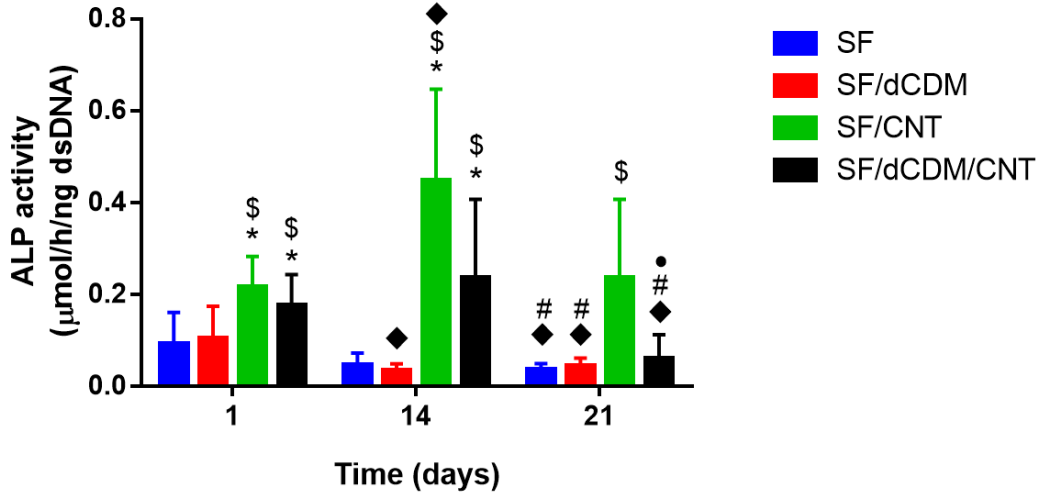
Figure 3.10 – Quantification of ALP activity of hASCs seeded on SF, SF/dCDM, SF/CNT and SF/dCDM/CNT scaffolds for 21 days. * - denotes statistically significant differences when compared to SF; # - denotes statistically significant differences when compared to SF/CNT; $ - denotes statistically significant differences when compared to SF/dCDM; ♦ - denotes statistically significant differences when compared to day 1; ● - denotes statistically significantly differences when compared to day 14. Data is presented as mean±stdev (n=9).

3.1.2.6. PCR analysis

The differentiation of hASCs seeded onto the scaffolds was analyzed by quantifying the relative gene expression of osteogenic-related markers Col Iα, Runx-2, OPN and ALP (Figure 3.11). SF/CNT and SF/dCDM/CNT scaffolds expressed significantly higher amounts of ALP than SF scaffolds for day 14. Moreover, on day 21 there was a significant decrease of ALP expression for SF/dCDM, SF/CNT and SF/dCDM/CNT scaffolds when compared to day 14 (Figure 3.11 A). For Runx-2, at day 14, SF/CNT and SF/dCDM/CNT scaffolds showed higher amounts of gene expression than SF scaffolds. When comparing day 14 with day 21, a significant increase was verified for SF scaffolds and a decrease for SF/dCDM/CNT scaffolds (Figure 3.11 B). The expression of Col Iα for day 14 showed significantly higher levels of expression for all conditions comparatively to SF scaffolds. Also a decrease was verified between day 14 and 21 for all conditions. For day 21, SF and SF/dCDM scaffolds present lower expression levels than SF/dCDM/CNT scaffolds (Figure 3.11 C). Finally, OPN transcript levels show significantly higher relative gene expression for SF/CNT scaffolds comparatively to the other conditions for day 14. At day 21, an increase of expression for SF scaffolds was verified. SF and SF/CNT scaffolds demonstrated higher expression than SF/dCDM and SF/dCDM/CNT at day 21 (Figure 3.11 D).
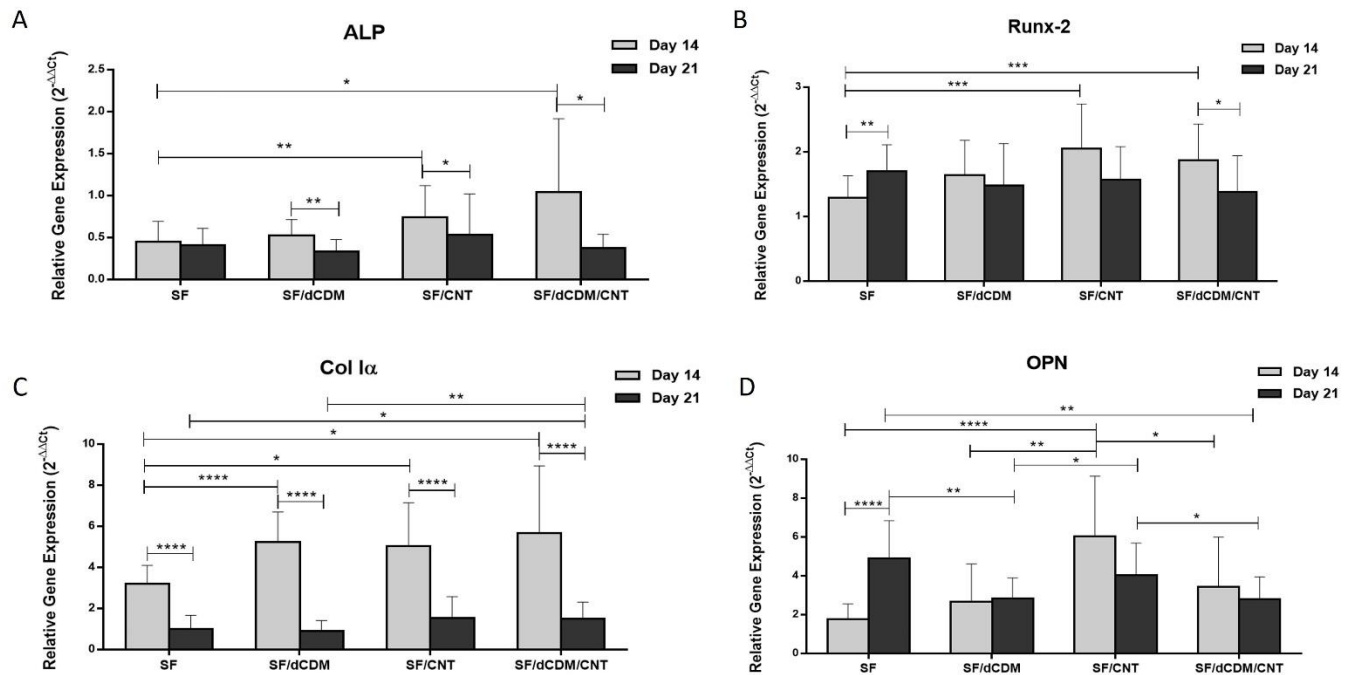
Figure 3.11 – Real time qRT-PCR analysis for different osteogenic associated genes. Relative expression of osteogenic-related transcripts, namely (A) ALP, (B) Runx-2, (C) Col Iα and (D) OPN, by the hASCs cultured on SF, SF/dCDM, SF/CNT and SF/dCDM/CNT scaffolds for 14 and 21 days. Fold changes in relative gene expression were calculated using the 2−ΔΔCt method. The significance levels were set to $p \leq 0.05$ (*), $p \leq 0.01$ (**), $p \leq 0.001$ (***) and $p \leq 0.0001$ (****).

3.1.2.7. Scaffolds hemocompatibility

Hemolytic assay was performed to assess the hemocompatibility of the scaffolds. For all four different formulations the obtained value of hemolysis percentage was 0% indicating no bursts of blood cells (Table 3.3).

Table 3.3 – Results of Hemolytic assay. Results of hemolytic assay on SF, SF/dCDM, SF/CNT and SF/dCDM/CNT scaffolds with PBS acting as negative control group (CTRL -) and Triton X-100 as positive control group (CTRL+).

Samples	Hemolysis (%)
SF	0
SF/dCDM	0
SF/CNT	0
SF/dCDM/CNT	0
CTRL-	0
CTRL+	100

3.2. Discussion

Currently, in bone tissue engineering (BTE) the natural step forward is the development of biomimetic approaches that recapitulate the native tissues environment ideal for regeneration of bone tissue (2). The existent scaffold approaches have not yet the specificity to mimic the different dimensions of the natural tissue. Hence, the challenge remains the development of more efficient hierarchical scaffolds.

In the present study, SF was combined with dCDM and CNT to produced hierarchical scaffolds, aiming the mimicry of the bone structure, from macro to nanoscale. These scaffolds were evaluated regarding their mechanical and structural properties, and their effects on cells behavior, namely viability, proliferation and differentiation along the osteoblastic lineage. Firstly, the efficient decellularization of the dCDM was verified by means of hematoxylin and eosin staining, to guarantee the absence of visible nuclei. This is of great importance since it prevents the occurrence of an immunological response and as such is critical for further application of the dCDM (3). Furthermore, Masson's Trichrome showed a clear preservation of collagen in the dCDM. Several studies have reported the importance of collagen on cellular differentiation since it contains several biological cues that can modulate cells adhesion, proliferation and differentiation (4). DNA quantification was also performed, demonstrating that the dsDNA content was below 50 ng/mg of matrix dry weight, the accepted threshold for effective decellularization (1).

Other important aspect for hierarchical scaffold production is their mechanical and structural properties. A minimum of pore size ranging from 100 μm to 150 μm has been described to be required for bone formation (5). Also, scaffolds should ideally possess between 60% - 90% of total porosity (6). The analysis of the scaffold's porosity showed that CNT appear to have a decreasing effect on pore size, since the SF/CNT scaffolds presented lowest pore size (63 ± 29 μm) and total porosity (60 ± 3%). On the other hand, the incorporation of dCDM seems to increase the pore size since SF/dCDM and SF/dCDM/CNT present a pore size of 135 ± 34 μm and 112 ± 22 μm respectively, countering the previous described effect of the CNT. The pore size observed was smaller than seen by Ribeiro *et al.* who used SF and HRP/H$_2$O$_2$ to fabricate scaffolds using enzymatic cross linking and salt leaching. In fact, they observed a mean pore size of 361.4 μm (7). This indicate that the chosen processing method can drastically influence pore size and the one chosen for this work successfully resulted in pores sizes within the described optimum range for bone formation. In a similar manner to pore size, total porosity increased with the presence of dCDM, to 76 ± 4% in the case of SF/dCDM and 75 ± 3% in the case of SF/CNT/dCDM. The results are in the same magnitude as that reported by Costa *et al.* that observed a 59.1% total porosity for SF scaffold (8). Besides these observations, micro-CT results also showed that CNT appear to be adequately dispersed through the scaffolds matrix. This observation is very important since CNT are predisposed to entangle and form agglomerates due to the presence of van der Waals forces between the tubes and such agglomeration may hinder its application (9).

Considering the mechanical analysis, although the positive effect on pore size, the conditions modified with dCDM showed a 10 times lower storage modulus than SF and SF/CNT scaffolds. The weaker mechanical properties can be explained by presence of collagen in the dCDM, as verified by the Masson's Trichrome, which is widely known to present low storage modulus (10,11). Furthermore, all scaffolds were found to be elastic as evidenced by the tan δ (<1) values. Results showed that even though the porosity of the conditions modified with dCDM is more suitable for bone regeneration, its incorporation also results in much weaker mechanical properties, very different from native bone tissue stiffness (e.g., ≈ 20 GPa in the case of cortical bone) (11). Interestingly, studies have shown that scaffolds with lower stiffness (< 0.7 kPa) were capable to stimulate cell proliferation and osteogenic differentiation at a higher level than stiffer scaffolds (> 5 kPa) (12,13). Thus, the scaffolds with dCDM are within the limit of the optimum scaffolds' stiffness values to promote the differentiation along the osteogenic lineage. Besides, scaffolds were soaked in SBF solution with the purpose of evaluating its bioactivity and thus foresee its behavior upon implanted in an *in*

vivo environment. SF scaffolds showed to be bioactive as expected since silk bioactivity is well known and widely studied (14). Regarding SF/dCDM/CNT scaffolds, the results showed a very similar bioactivity to SF scaffolds, suggesting that the addition of dCDM and CNT did not affect the SF bioactivity.

The effect of the developed scaffolds on cells was studied using hASCs cultured without supplemented medium, namely in terms of cell adhesion and spreading, metabolic activity, cell proliferation, ALP activity and gene expression. Cells seeded on SF, SF/dCDM and SF/CNT scaffolds evidenced an increase in metabolic activity across all time points, in opposition to SF/dCDM/CNT scaffolds where the metabolic activity decreased from day 1 to day 14. Additionally, for SF/dCDM/CNT, between day 14 and day 21 the stagnation of metabolic activity is consistent with the stagnated cell proliferation which indicates that cells were beginning to differentiate along the osteoblastic lineage. In fact, it is widely accepted that when cells begin to differentiate, they become less proliferative as observed between day 14 and day 21 (15). Interestingly, between day 1 and day 14, SF/dCDM evidencing the highest cell proliferation rate, which could be related to of the presence of dCDM. In fact, it is described in the literature that scaffolds with cell-derived matrices present improved cell proliferation rates (16,17). Moreover, the lower stiffness of the scaffolds can result as well in improved cell proliferation (12). SEM images showed that the scaffolds were completely covered in cells with a high degree of confluence corroborating that cells were able to proliferate along the time of culture. This was further evidenced by Phalloidin-DAPI images, where cell elongation and random cell orientation could be seen. Additionally, live-dead analysis showed that scaffolds had no deleterious effects on cells across the 21 days of culture. In accordance to the previous results, HE staining also evidenced cell adhesion and spreading across the surface with some level of penetration into the scaffold interior. Furthermore, Masson's Trichrome showed the presence of *de novo* collagen in all conditions except SF/CNT, indicating that cells were capable to produce and secrete their own endogenous collagenous matrix at their pericellular space. These results suggest that CNT by itself may have a negative effect on collagen production, which can be countered by the presence of dCDM. In fact, in conditions containing dCDM, cells were capable to express collagen even in the presence of CNT. This observation contradicts the predominant trend on effects of CNT on the production of collagen described in the literature since multiple studies have found that CNT has a positive effect on collagen production (18,19). Taking this observations in consideration, further analysis will be necessary to better understand this result.

Regarding the evaluation of osteogenic differentiation, ALP, an early marker for osteogenic differentiation and normally present in high concentrations in growing bone, was assessed (20). ALP activity of cells seeded on SF/CNT and SF/dCDM/CNT scaffolds expressed the typical peak activity on day 14 with following decrease, as expected, suggesting that cells were differentiating along the osteoblastic lineage (21). Furthermore, It is well known and accepted that a decrease in ALP expression is associated with differentiation and mineralization (21). In this reasoning, the higher ALP activity observed on cells seeded on SF/CNT and SF/dCDM/CNT scaffolds might suggest a greater osteogenic potential. These results are in accordance with previous studies who showed enhanced ALP activity in carbon nanotubes modified scaffolds (22). It is further important to highlight that although dCDM had a visible positive effect on cell proliferation the same was not verified for ALP activity. This result was not expected since the evidences found in the literature indicate that cell-derived matrices have a positive effect on the ALP activity (16), for so, further investigation will be needed to clarify such results.

As regards of gene expression levels, different osteogenic markers were assessed, namely Runx-2, ALP, OPN and Col Iα. In the case of ALP and Runx-2, early markers of osteogenic differentiation, the results showed that these genes were expressed at day 14, decreasing at day 21, as expected from early expression markers (23,24). Thus, the increased expression for SF/CNT and SF/dCDM/CNT suggests that the addition of CNT stimulates osteogenic cell differentiation. In accordance to these results, other studies have found that the use of CNT upregulates Runx-2 gene expression (25) the same effect has also been observed for ALP expression (26). In the case of OPN, important in bone modeling (27) and collagen production (28), SF/dCDM/CNT and SF/CNT are the only conditions that displayed a pattern of early expression. Furthermore, at day 14, the OPN expression is lower for SF/dCDM/CNT condition comparatively to SF/CNT, this could suggest that cells cultured on SF/dCDM/CNT scaffolds were further advanced in the differentiation stage. Additionally, and in accordance with other studies an upregulation on conditions with CNT was also observed (25). For Col Iα, a marker of osteogenic differentiation related to bone formation and bone architecture (29), the results showed higher expression on SF/dCDM, SF/CNT and SF/dCDM/CNT then on simple SF scaffolds. This result suggest that the osteogenic potential of these scaffolds is superior as compared to the control. It is important to highlight that SF/CNT and SF/dCDM/CNT possesses significant higher gene expression for all four genes comparatively to the plain SF scaffolds, suggesting an earlier cellular osteogenic differentiation and higher osteogenic potential than the SF scaffold.

Finally, the hemolytic assay was performed to evaluate hemoglobin release in the plasma (as an indicator of red blood cell lysis) on all conditions. According to Testing and Materials a material is considered safe when its hemolysis percentage is under 2%, while a 5% limit is specified by ISO 10 993-5 (30,31). Results showed no hemolytic effect for any of the scaffolds. Hence, the findings show that the scaffolds are hemocompatible making them suitable materials for further *in vivo* applications.

Acknowledgments

3.3. References

1.   Crapo PM, Gilbert TW, Badylak SF. An overview of tissue and whole organ decellularization processes. Biomaterials. 2011;32(12):3233–43.

2.   Du Y, Guo JL, Wang J, Mikos AG, Zhang S. Hierarchically designed bone scaffolds: From internal cues to external stimuli. Biomaterials. 2019/07/03. 2019 Oct;218:119334.

3.   Choudhury D, Yee M, Sheng ZLJ, Amirul A, Naing MW. Decellularization systems and devices: State-of-the-art. Acta Biomater. 2020;115:51–9.

4.   Rico-Llanos GA, Borrego-González S, Moncayo-Donoso M, Becerra J, Visser R. Collagen Type I Biomaterials as Scaffolds for Bone Tissue Engineering. Polymers (Basel). 2021 Feb 17;13(4):599.

5.   Bose S, Vahabzadeh S, Bandyopadhyay A. Bone tissue engineering using 3D printing. Mater Today. 2013;16(12):496–504.

6.   Marew T, Birhanu G. Three dimensional printed nanostructure biomaterials for bone tissue engineering. Regen Ther. 2021 May 28;18:102–11.

7.   Ribeiro VP, da Silva Morais A, Maia FR, Canadas RF, Costa JB, Oliveira AL, et al. Combinatory approach for developing silk fibroin scaffolds for cartilage regeneration. Acta Biomater. 2018;72:167–81.

8.   Costa JB, Silva-Correia J, Oliveira JM, Reis RL. Fast Setting Silk Fibroin Bioink for Bioprinting of Patient-Specific Memory-Shape Implants. Adv Healthc Mater. 2017 Nov 1;6(22):1701021.

9.   Liang C, Wang B, Chen J, Yong Q, Huang Y, Liao B. Dispersion of Multi-Walled Carbon Nanotubes by Polymers with Carbazole Pendants. J Phys Chem B. 2017 Sep 7;121(35):8408–16.

10.   Wu C-C, Ding S-J, Wang Y-H, Tang M-J, Chang H-C. Mechanical properties of collagen gels derived from rats of different ages. J Biomater Sci Polym Ed. 2005;16(10):1261–75.

11.   Guimarães CF, Gasperini L, Marques AP, Reis RL. The stiffness of living tissues and its implications for tissue engineering. Nat Rev Mater. 2020;5(5):351–70.

12.   Zhang J, Wehrle E, Adamek P, Paul GR, Qin X-H, Rubert M, et al. Optimization of mechanical stiffness and cell density of 3D bioprinted cell-laden scaffolds improves extracellular matrix mineralization and cellular organization for bone tissue engineering. Acta Biomater. 2020;114:307–22.

13.   Maia FR, Fonseca KB, Rodrigues G, Granja PL, Barrias CC. Matrix-driven formation of mesenchymal stem cell-extracellular matrix microtissues on soft alginate hydrogels. Acta Biomater. 2014 Jul;10(7):3197–208.

14.   Zhang H, You R, Yan K, Lu Z, Fan Q, Li X, et al. Silk as templates for hydroxyapatite biomineralization: A comparative study of Bombyx mori and Antheraea pernyi silkworm silks. Int J Biol Macromol. 2020 Dec;164:2842–50.

15.   Ruijtenberg S, van den Heuvel S. Coordinating cell proliferation and differentiation: Antagonism

between cell cycle regulators and cell type-specific gene expression. Cell Cycle. 2016;15(2):196–212.

16.   Kim IG, Hwang MP, Du P, Ko J, Ha C, Do SH, et al. Bioactive cell-derived matrices combined with polymer mesh scaffold for osteogenesis and bone healing. Biomaterials. 2015 May;50:75–86.

17.   Assunção M, Dehghan-Baniani D, Yiu CHK, Später T, Beyer S, Blocki A. Cell-Derived Extracellular Matrix for Tissue Engineering and Regenerative Medicine. Front Bioeng Biotechnol. 2020;8:602009.

18.   Sá MA, Ribeiro HJ, Valverde TM, Sousa BR, Martins-Júnior PA, Mendes RM, et al. Single-walled carbon nanotubes functionalized with sodium hyaluronate enhance bone mineralization. Brazilian J Med Biol Res = Rev Bras Pesqui medicas e Biol. 2015/12/04. 2016 Feb;49(2):e4888–e4888.

19.   Andrade VB, Sá MA, Mendes RM, Martins-Júnior PA, Silva GAB, Sousa BR, et al. Enhancement of Bone Healing by Local Administration of Carbon Nanotubes Functionalized with Sodium Hyaluronate in Rat Tibiae. Cells Tissues Organs. 2017;204(3–4):137–49.

20.   Zhou T, Chen S, Ding X, Hu Z, Cen L, Zhang X. Fabrication and Characterization of Collagen/PVA Dual-Layer Membranes for Periodontal Bone Regeneration. Front Bioeng Biotechnol. 2021;9:630977.

21.   Jaiswal N, Haynesworth SE, Caplan AI, Bruder SP. Osteogenic differentiation of purified, culture-expanded human mesenchymal stem cells in vitro. J Cell Biochem. 1997 Feb;64(2):295–312.

22.   Pan L, Pei X, He R, Wan Q, Wang J. Multiwall carbon nanotubes/polycaprolactone composites for bone tissue engineering application. Colloids Surfaces B Biointerfaces. 2012;93:226–34.

23.   Yong KW, Choi JR, Choi JY, Cowie AC. Recent Advances in Mechanically Loaded Human Mesenchymal Stem Cells for Bone Tissue Engineering. Int J Mol Sci. 2020 Aug 13;21(16):5816.

24.   Radwan-Pragłowska J, Janus Ł, Piątkowski M, Bogdał D, Matysek D. 3D Hierarchical, Nanostructured Chitosan/PLA/HA Scaffolds Doped with TiO(2)/Au/Pt NPs with Tunable Properties for Guided Bone Tissue Engineering. Polymers (Basel). 2020 Apr;12(4).

25.   Liu X, George MN, Park S, Miller Ii AL, Gaihre B, Li L, et al. 3D-printed scaffolds with carbon nanotubes for bone tissue engineering: Fast and homogeneous one-step functionalization. Acta Biomater. 2020 Jul;111:129–40.

26.   Li X, Liu H, Niu X, Yu B, Fan Y, Feng Q, et al. The use of carbon nanotubes to induce osteogenic differentiation of human adipose-derived MSCs in vitro and ectopic bone formation in vivo. Biomaterials. 2012 Jun;33(19):4818–27.

27.   Bonventre J V, Sabbisetti V. Chapter 48 - Acute Kidney Injury: Biomarkers from Bench to Bedside. In: Himmelfarb J, Sayegh Dialysis, and Transplantation (Third Edition) MHBT-CKD, editors. Philadelphia: W.B. Saunders; 2010. p. 668–76.

28.   Marra F, Caligiuri A. Chapter 5 - Cytokine Production and Signaling in Stellate Cells. In: Gandhi CR, Pinzani MBT-SC in H and D, editors. Boston: Academic Press; 2015. p. 63–86.

29.   Hayrapetyan A, Bongio M, Leeuwenburgh SCG, Jansen JA, van den Beucken JJJP. Effect of Nano-HA/Collagen Composite Hydrogels on Osteogenic Behavior of Mesenchymal Stromal Cells. Stem

cell Rev reports. 2016 Jun;12(3):352–64.

30.   Weber M, Steinle H, Golombek S, Hann L, Schlensak C, Wendel HP, et al. Blood-Contacting Biomaterials: In Vitro Evaluation of the Hemocompatibility. Front Bioeng Biotechnol. 2018;6:99.

31.   Zhou HY, Zhang YP, Zhang WF, Chen XG. Biocompatibility and characteristics of injectable chitosan-based thermosensitive hydrogel for drug delivery. Carbohydr Polym. 2011;83(4):1643–51.

CHAPTER IV.

General Conclusion and Future Directions

CHAPTER IV. General Conclusions and Future Directions

4.1. General Conclusions and Future Directions

Bone tissue comprises a complex hierarchical structure, crossing nanoscale to macroscale, which provides distinct properties like high mechanical strength. Worldwide, bone tissue engineers have pursued different biomimetic approaches to recapitulate the native bone tissue microenvironment, envisioning the production of functional bone tissue. Despite the difficulty in mimicking the bone architecture and intrinsic properties *in vitro*, studies have been shown that hierarchical scaffolds present high potential to regenerate bone tissue. In this sense, the internal cues comprised within hierarchical scaffolds have the ability to induce bone regeneration. The ECM has gained increasing interest in recent years as an optimal biomaterial for tissue engineering. Its importance in cell proliferation and tissue structure has long been known, but recent development in decellularization methods have made its manipulation and controlled use possible. Hence, due to its natural characteristics, it stands to reason that the use of decellularized ECM is of immense potential for future bone tissue engineering breakthroughs.

With this in mind, the present work intended to develop scaffolds with a multifaceted hierarchical structure, comprising biomimetic cues within different scale ranges. For that, new scaffolds consisting of 8% SF, 1 mg/ml of dCDM and/and 1 mg/ml of CNT were prepared, envisioning the production of scaffolds not only with improved mechanical properties, but also improved biological cues. The developed SF/dCDM/CNT scaffolds revealed great potential for bone tissue engineering applications in the performed tests, as demonstrated by the expression of osteogenic markers, suitable hemocompatibility, and good biomineralization and improved mechanical properties. Nevertheless, in future studies it will be essential to test the developed scaffolds using clinically relevant models, to evaluate their long-term effects and stability in bone defects. Taking these results in consideration, future studies focused on the ability of SF to form anisotropic structure to create guided architectures more suited for bone growth, could be an interesting approach to convey an additional biomimetic dimension to the scaffold system. Moreover, carbon nanotubes electrical stimulation can accelerate bone formation, regeneration, ECM protein synthesis, and enhance osteogenic markers expression. The investigation of this interesting property when incorporated into a scaffold

system and its effects on cells and the different scaffold materials could enhance the osteogenic potential of these scaffolds. Additionally, functionalization of CNT may facilitate the incorporation of extra biochemical cues into the scaffolds. This could open the way for potential drug delivery strategies that could further complement the dCDM components. Such improvements may improve the interaction of develop scaffolds with the surrounded bone defect environment. In fact, further investigation regarding the interaction mechanisms between scaffolds and surrounded tissues should be given to clarify how the implanted cues influence the bone regeneration process, namely regarding the development of blood vessels and nerve fibers. It is known that the presence of both is crucial for the development of functional bone tissue, but most often one or the other is disregarded when designing hierarchical scaffolds. Blood vessels are crucial to supply the nutrients and oxygen to promote the formation of nerve fibers, which in turn deliver the necessary factors to enhance vascularization. This interplay favors bone regeneration. The limited studies regarding such subject are mainly due to the struggle towards creating a neurovascularized network within scaffolds that present hard tissue properties. In this regard, an improved understanding about blood vessels and nerves interactions within bone tissue is crucial, enabling to introduce such bioinspired cues into scaffold design and consequently enhance its successful implantation.

Additionally, the inclusion of precise features to meet patient microenvironmental specificities is essential to the successful engraftment upon scaffold implantation. For example, considering bone resections, it would be important to include tumor inhibition cues besides bone regeneration cues.

Overall, further studies regarding bone tissue hierarchical structure would be valuable to develop improved scaffold designs capable to meet the multiscale biological and physical cues of patient's bone tissue and consequently induce the formation of functional bone tissue.